Computing Magnetic Susceptibility Maps from Gradient Recalled Echo MRI for use in Multiple Sclerosis Studies

A Thesis

Presented in Partial Fulfillment of the Requirements for the Degree Bachelor of Science in Electrical and Computer Engineering with Distinction in Electrical and Computer Engineering in the College of Engineering at The Ohio State University

By

Grant Kaijuin Yang

* * * * *

The Ohio State University

2013

Approved by

Professor Bradley Clymer

Co-Advisor

Professor Petra Schmalbrock

Co-Advisor

Department of Electrical and Computer Engineering

ABSTRACT

Multiple sclerosis (MS) is an autoimmune disease in which myelin in the central nervous system is destroyed. The MS progression is tracked by characterizing the lesions caused by the demyelination and subsequent destruction of nerve cells. The pattern of iron deposition within MS lesions has been thought to indicate specific processes in MS pathology. A method of visualizing and quantifying iron in MS lesions would provide additional insight into the inflammatory process in multiple sclerosis, and assist in assessing the effectiveness of current medications. Developments in high field magnetic resonance (MR) phase imaging have shown promise as a method of generating quantitative susceptibility maps, which can be correlated to iron concentration in the brain. However, current methods for processing MRI phase images suffer from artifacts and/or are restricted by computational intensity.

The implementation and verification of a new method for generating magnetic susceptibility maps using a Wiener deconvolution based filter was developed and tested. Given the phase image, the proposed algorithm calculates the susceptibility distributions in the frequency domain. The Wiener deconvolution addresses reconstruction artifacts by filtering the frequency domain transfer function, attenuating frequencies with low signal to noise ratio (SNR). This approach has been shown to reduce streaking artifacts and noise in the susceptibility map, while retaining the advantage of fast computation in the frequency domain. The numerical accuracy of the algorithm was verified using in vivo brain images, phantom data with known susceptibilities, and

numerical phantoms. The QSM algorithm will be applicable to several longitudinal studies of the effectiveness of several drugs for the treatment of MS.

This is dedicated to my family and all those who suffer from multiple sclerosis.

ACKNOWLEDGMENTS

This project would not have been possible without the help and guidance of my advisors, Professor Petra Schmalbrock and Professor Bradley Clymer. Their advise, expertise, and encouragement throughout the project was indispensible. I would like to thank them for the time they dedicated to helping me develop this thesis. I would also like to thank Dr. David Pitt for his collaborating on this project. Without your medical expertise and patients, this thesis would not have been possible. I would also like to thank my coworkers at the Wright Center of Innovation in Biomedical Imaging for providing an engaging and encouraging environment in which to work on my project. Credit also goes to my wonderful family for their encouragement and support throughout this project. I would not be where I am today without you.

VITA

January 31, 1991…….……Born – Columbus, Ohio, USA

Autumn 2009……...Began Undergraduate Studies,
The Ohio State University

Spring 2013 ……..B.S., The Ohio State University

TABLE OF CONTENTS

Page

LIST OF FIGURES

Figure **Page**

CHAPTER 1

INTRODUCTION

1.1 Motivation

Multiple sclerosis (MS) is a neurodegenerative disease of the central nervous system. The disease is characterized by the destruction of myelin, which coats and protects the axons of nerve cells. The primary mechanism behind MS is believed to be autoimmune inflammation [1]. Intracellular iron is a key component in regulating the function of inflammation in the central nervous system. While iron is toxic at high concentrations, it is required for the synthesis of myelin by oligodendrocytes. Due to iron's critical role in the inflammatory process and also in the function of the central nervous system, iron is believed to play a critical role in multiple sclerosis.

Iron is retained by macrophages during the inflammation, and their presence in MS lesions is a potential indicator of inflammatory activity, and the underlying mechanisms behind MS. Recent research suggests activation phenotypes of macrophages present in MS lesions can be determined by measuring the iron concentration. There are two major activation phenotypes of macrophages: proinflammatory or M1 macrophages, and anti-inflammatory or M2 macrophages. M1 macrophages secrete high levels of proinflammatory cytokines and are responsible for microbicidal capabilities, while M2 macrophages inhibit proinflammatory cytokines and play a

role in tissue repair [2]. M1 macrophages are characterized by high intracellular iron concentration, while M2 macrophages are characterized by lower intracellular iron concentrations. Recent research has shown that iron uptake in M1 macrophages may enhance the inflammatory responses, preventing macrophages from converting to the M2 phenotype thus slowing tissue repair and recovery. Elevated levels of iron in active MS lesions have been found in preliminary pathology and MRI results, and a subset of lesions are shown in tissue specimen to exhibit a ring around the lesion periphery of elevated iron levels [2]. This supports the hypothesis that iron is at least an indicator, if not a causative agent, in MS. Developing methods for quantifying and visualizing iron concentrations in the brain using MR phase imaging would provide a new way to assess the inflammatory status of MS patients, and aid advances in treatment.

1.2 MRI

Demyelination results in tell-tale lesions and the formation of astrocytic scars due to axonal loss. These lesions are routinely imaged using magnetic resonance imaging (MRI). T2-weighted imaging is sensitive to hyperintensities in white matter corresponding to edemas, mild demyelination, and lesions caused by the destruction of neurons and glial cells. In addition to T2-weighted imaging, Gadolinium (Gd) enhanced T1-weighted imaging can be used to delineate areas of acute inflammatory activity resulting in a breakdown of the blood brain barrier. Although a general picture of MS activity is provided by the combination of T1 and T2 weighted imaging, these traditional techniques do not provide a quantitative analysis of the amount of inflammation present in each individual lesion. Gd-enhanced imaging only accounts for a small subset of active lesions, and enhancement usually only occurs for a fraction of the inflammatory process.

Recent research suggests that magnetic resonance imaging (MRI) can be used to quantify iron concentrations in MS lesions *in vivo* for a better understanding of the etiologic mechanisms behind MS[1]. The complex signal that forms an MRI is induced by the excitation of protons spinning due to the presence of the scanner's magnetic field. Conventional MRI is formed by the magnitude of the signal, but the phase can be used to acquire additional information, which can be used to calculate iron content. The frequency of the proton's spins can be altered by small changes in the magnetic field. These magnetic field inhomogeneities can be detected as variations in the phase of the MRI. Magnetic field inhomogeneities arise from three sources: inhomogeneities within the main magnetic field (B_0), radiofrequency pulse inhomogeneities (B_1), and local field inhomogeneities due to intrinsic tissue properties such as magnetic susceptibility, the degree of magnetization of a material in response to an applied magnetic field. Acquiring meaningful images of the intrinsic tissue properties requires the removal of B_0 and B_1 inhomogeneities from the phase image, leaving the local field shifts due to changes in magnetic susceptibility. *In vivo* iron is paramagnetic; therefore increased iron concentrations will raise the magnetic susceptibility of the tissue. In order to quantify the iron concentration from the local field inhomogeneities, quantitative susceptibility maps (QSM), which show the iron distribution that caused the local field changes, must be generated. Developing methods for quantifying and visualizing iron concentrations in the brain using MR phase imaging would provide a new way to assess the inflammatory status of MS patients and the efficacy of new treatment options.

1.3 Problem Statement

Quantifying iron content in the brain using MRI is a challenging problem. Accurate quantification of iron from phase imaging requires careful removal of non-tissue phase effects such as B_1 and B_0 inhomogeneities. Furthermore, the inverse problem from field shift to susceptibility is an ill-posed inverse problem. The goal of this project is to develop, validate and compare various methods for generating QSM images in order to find the optimum solution for use in a longitudinal study of inflammation in MS.

1.4 Organization

In Chapter 2 of this thesis, the role of susceptibility in MR imaging is discussed. The effect of susceptibility on the phase of the MR signal is detailed culminating in the formulation of the inverse problem calculating susceptibility from phase of the MR signal. In Chapter 3, a comparison of field inhomogeneity removal methods is conducted. In Chapter 4, various solutions to the inverse QSM problem are presented including a new *k*-space filter based on the Wiener deconvolution. A summary of the results of these studies as well as suggestions for future work has been included in Chapter 6.

CHAPTER 2

MAGNETIC SUSCEPTIBILITY IN MRI

2.1 Overview

Magnetic resonance imaging is inherently sensitive to distortions in the magnetic field caused by magnetic susceptibility differences between various tissues. Understanding the fundamentals of magnetic susceptibility allows the use of MRI to measure important tissue properties such as iron content. In this chapter, the physical principles of magnetic susceptibility are described, and the effect on the magnetic field of an arbitrary susceptibility distribution is calculated. Finally, the magnetic susceptibility of tissue is related to the phase of the gradient echo magnetic resonance image.

2.2 Magnetic Susceptibility

2.2.1Definition of Magnetic Susceptibility

Magnetic susceptibility is the tendency of a material to distort a magnetic field. This is described mathematically as $M = \chi H$, where M is the magnetization of a material, H is the magnetic field strength, and χ is the susceptibility. The susceptibility of a material is directly related to its relative permeability. This can be seen by relating the magnetization and magnetic field strength to the magnetic flux density as seen in equation 2.1-2 below.

$$B = \mu_0(H + M) \tag{2.1}$$

$$B = \mu_0\mu_r H \tag{2.2}$$

Combining equations 2.1 and 2.2, susceptibility is equal to $\mu_r - 1$. When dealing with weakly magnetic materials such as tissue, it is much more convenient to use susceptibility rather than relative permeability, since $|\chi| \ll 1$.

2.2.2 Mechanisms of Magnetic Susceptibility

The primary mechanism of magnetic susceptibility is known as Langevin diamagnetism. Langevin diamagnetism results from a change in the orbital motion of the electrons around the atom in the presence of an external magnetic field. The change in motion induces a magnetic field that is opposed to the applied field. This results in a weak, negative magnetization that is temperature independent and present in all molecules. In transition metals, a similar effect is produced by the movement of conducting electrons through the lattice. This phenomenon is known as the Landau diamagnetism.

Paramagnetism results from the alignment of conduction electron spins in metallic atoms. The effect is known as Pauli paramagnetism, and in the case of ferromagnetic materials, it is known as the alignment of ferromagnetic domains. The tendency of the unpaired electrons to align with the magnetic field is offset by thermal agitation of the electrons, which produces a random spin orientation. Thus, paramagnetism due to spin alignment of electrons is dependent on temperature, an effect known as Curie's Law. Pauli and Curie paramagnetism are much stronger than the Langevin or Landau diamagnetism, and are responsible for the high susceptibility of ferrous compounds.

2.2.3 Tissue Susceptibility

Because the predominant component of most tissues is water, most tissues have susceptibilities within 10-20% that of water; ie: -11 ppm to -7 ppm[3]. The deviation is largely due to the presence of trace amounts of paramagnetic iron compounds. While the effect of the low concentrations of iron compounds is small throughout most of the body, tissues which store iron such as the basal ganglia of the brain show a significant susceptibility shift compared to the surrounding tissue. Iron ions in the human body consist primarily of hemoglobin, ferritin and hemosiderin. Deoxyhemoglobin is found in blood, and consists of four protein chains each containing a Fe^{2+} ion. The susceptibility shift caused by a single deoxyhemoglobin molecule is approximately +.2 ppm[3]. Ferritin and hemosiderin are proteins found in macrophages which store iron as Fe^{3+}. The concentration of iron of wet tissue can be calculated from its susceptibility shift according to equation 2.3 below, where *c* is the iron concentration in mg iron per gram of tissue, and ρ is the tissue density in g/cm^3[3].

$$\chi = \chi_{water} + (1.30 \times 10^{-6})c\rho \tag{2.3}$$

The ability to quantify the amount of iron stored in tissue is extremely useful for applications in multiple sclerosis where the storage of iron has been correlated to inflammatory activity.

2.3 The Effect of an Arbitrary Susceptibility Distribution on the Magnetic Field

The effect of an arbitrary susceptibility distribution on the magnetic field can be calculated from Maxwell's equations [4][5]. According to Maxwell's equations, the curl of the magnetic field strength is equal to the conduction current density:

$$\nabla \times \vec{H} = \vec{J}_c \tag{2.4}$$

Assuming negligible eddy currents, the conduction current density in MR applications is close to zero. This allows for the existence of a magnetic potential, Φ, such that

$$\vec{H} = -\nabla\Phi \tag{2.5}$$

From Gauss's law for magnetism, the divergence of the magnetic induction is always zero.

$$\nabla \cdot \vec{B} = -\mu_0 \nabla \cdot \left((1+\chi)\vec{H}\right) = 0 \tag{2.6}$$

Substituting the equation for the magnetic potential into equation 6 yields

$$\nabla \cdot \left((1+\chi)\nabla\Phi\right) = 0 \tag{2.7}$$

By the product rule, equation 2.7 is equivalent to

$$\nabla\chi \cdot \nabla\Phi + (1+\chi)\nabla^2\Phi = 0 \tag{2.9}$$

For MR applications, the magnetic field strength is the sum of the uniform magnetic field, $\vec{H}_0 = (0,0,H_0)$, inhomogeneities in the magnet field, $\vec{h}_{in}$, and the inhomogeneities introduced by variations in the susceptibility of objects in the field, $\vec{h}_{obj}$.

$$\vec{H} = \vec{H}_0 + \vec{h}_{in} + \vec{h}_{obj} \tag{2.10}$$

The magnetic potential can be rewritten as the sum of these terms:

$$\Phi = \Phi_0 + \Phi_{in} + \Phi_{obj},\ \Phi_0 = -H_0 \cdot z \tag{2.11}$$

Combining equations 2.9 and 2.11, gives equation 2.12:

$$-\frac{\delta\chi}{\delta z}H_0 - \nabla\chi \cdot \left(\vec{h}_{in} + \vec{h}_{obj}\right) + (1+\chi)\left(\nabla^2\Phi_{in} + \nabla^2\Phi_{obj}\right) = 0 \tag{2.12}$$

Since equation 2.12 must hold when $\chi = 0$, $\nabla^2\Phi_{in}$ must also equal zero. In MR applications $H_0 \ll \vec{h}_{obj}, \vec{h}_{in}$ and $\chi \ll 1$ yielding equation 2.13 below.

$$\frac{\delta\chi}{\delta z}H_0 = \nabla^2\Phi_{obj} \tag{2.13}$$

From equation 2.13, the form of solution to the partial differential equation for the magnetic gradient is of the same form as the Poisson equation for electrostatic potential:

$$FT\left(\Phi_{obj}\right) = -j \cdot H_0 \cdot \frac{k_z}{k_x^2+k_y^2+k_z^2} \cdot FT(\chi) \tag{2.14}$$

Equation 2.14 can be rewritten in terms of the field strength as shown below:

$$FT\left(\vec{h}_{obj}\right) = -H_0 \cdot \frac{k_z^2}{k_x^2+k_y^2+k_z^2} \cdot FT(\chi) \tag{2.15}$$

The magnitude of the magnetic induction experienced by a nucleus can be written as:

$$\vec{B}_{nuc} \cong \left(1 - \frac{2}{3}\chi\right) \cdot (1+\chi)\mu_0\vec{H} \tag{2.16}$$

when the effect of the electron shell around the nucleus is neglected, and the nucleus is assumed to be in a small sphere of Lorentz.

Neglecting second order components of $\vec{H}$ and approximating the induction effect only along the z-direction gives:

$$\vec{B}_{nuc} \cong B_{nuc,z} \cong \mu_0\left(\left(1 + \frac{1}{3}\chi\right) \cdot H_0 + h_{in,z} + h_{obj,z}\right) \tag{2.17}$$

Substituting equation 2.17 into 2.15 gives an equation for calculating the field perturbation at a point in space due to an arbitrary susceptibility distribution as a point by point multiplication in the spatial frequency domain.

$$B_{nuc,z} = B_0 + B_{in} + B_0 FT^{-1}\left\{\left(\frac{1}{3} - \frac{k_z^2}{k_x^2+k_y^2+k_z^2}\right) FT(\chi)\right\} \quad (2.18)$$

Since equation 2.18 allows calculation in the spatial frequency domain, calculations are much faster than the equivalent integral solutions which represent a convolution in the spatial domain[4].

$$B_{nuc}(\vec{r}) = \frac{B_0}{4\pi}\int \frac{\chi(\vec{r})\left(3\cos^2\theta - 1\right)}{|\vec{r}' - \vec{r}|^3} d^3\vec{r}' \quad (2.19)$$

$$B_{nuc}(\vec{r}) = B_0(\chi * d)(\vec{r}), \text{ '*' denotes a 3D convolution} \quad (2.20)$$

Although seldom calculated explicitly as a convolution, it is important to recall the relationship between convolution in the spatial domain and point by point multiplication in the frequency domain when constructing QSM algorithms.

2.4 GRE Pulse Sequence

MRI relies on differing relaxation properties between tissues to provide image contrast. In the presence of a magnetic field, the spins of the hydrogen protons align with the main magnetic field in their low energy state. During an imaging sequence, the spins are excited from the low energy state by an RF pulse by flipping the proton spins from the longitudinal z-direction into the transverse or xy plane as shown in Figure 2.1 below.

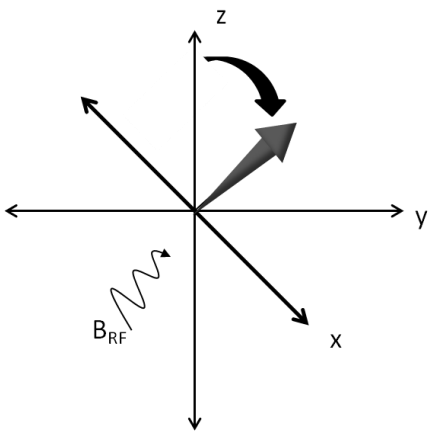

Figure 2.1: RF excitation of proton spins from the longitudinal plane to the transverse plane

The MR signal is generated by the decay of the proton back to steady state magnetization. The free induction decay of the MR signal is divided into two different mechanisms: spin-lattice relaxation and spin-spin relaxation. Spin-lattice relaxation is the return of the longitudinal magnetization after the RF excitation caused by dissipation of the RF energy due to vibrations and rotations in the lattice. Spin-lattice relaxation is governed by the time constant, T1. Spin-spin relaxation causes decay in the MR signal due to dephasing of the proton spins in the transverse planes. The spin-spin relaxations are caused by interactions between the spins of adjacent protons, and is governed by the time constant T2. In addition to the intrinsic tissue properties which cause T2 decay, the transverse magnetization is also dephased by susceptibility variations in the patient's body as well as magnetic field inhomogeneities. This component of spin-spin relaxation is governed by the time constant T2'. The total effect of spin-spin relaxation is additive and governed by the time constant $\frac{1}{T2^*} = \frac{1}{T2} + \frac{1}{T2'}$. The spin-lattice and spin-spin relaxations are depicted in Figure 2.2 below.

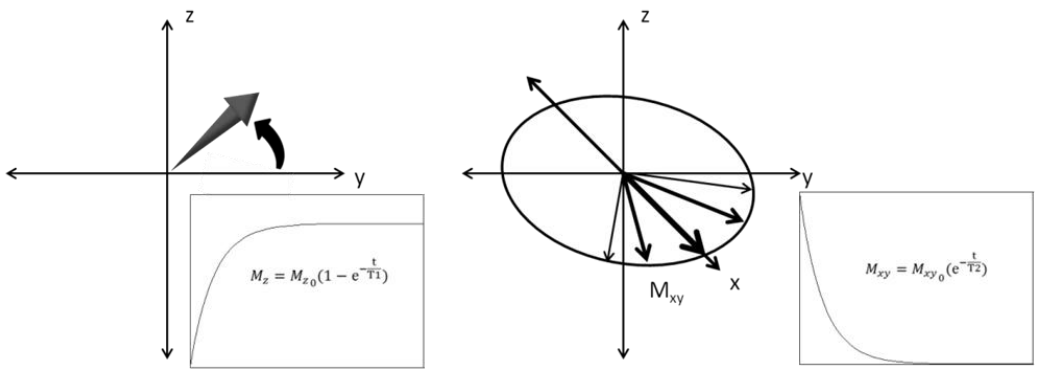

Figure 2.2: Spin-lattice relaxation (left), Spin-spin relaxation (right)

The dephasing effect of T2' relaxation can be measured using a gradient recalled echo (GRE) MR imaging sequence. The MR image is spatially encoded by applying magnetic field gradients across the object in order to introduce frequency and phase gradients in the acquired signal. In the frequency encode direction the phase shift introduced by the magnetic field gradient must be removed.

In a gradient echo sequence, a bipolar frequency encode gradient is used to refocus the spins to form a signal echo as shown in Figure 2.3 below.

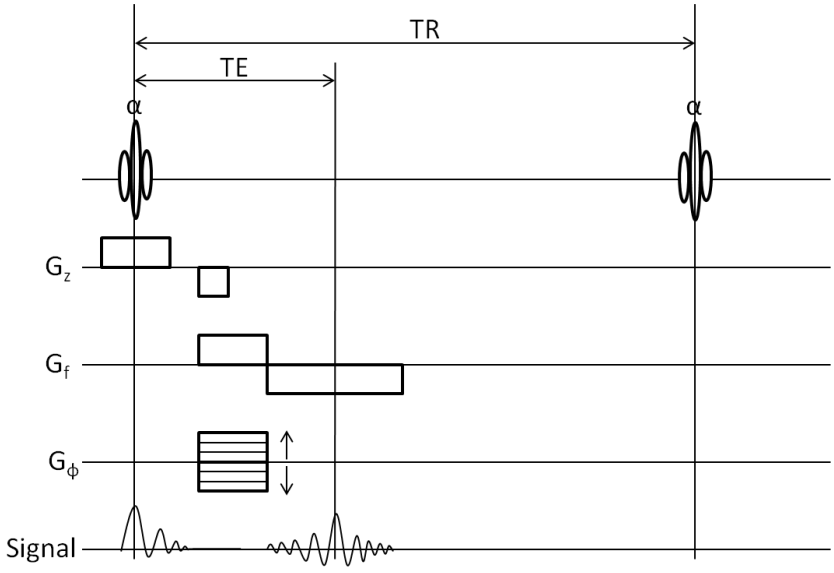

Figure 2.3: Gradient recalled echo imaging sequence

Unlike a spin echo sequence, a gradient echo sequence is sensitive to T2' effects, because the bipolar gradient only removes the dephasing effect of the frequency encode gradient. The dephasing effect due to magnetic field inhomogeneities and tissue susceptibilities remains and propagates linearly with time according to equation 2.21 below where ϕ is the phase of the MR signal, γ is the gyromagnetic ratio, ΔB is a local field shift due to T2' effects, and TE is the echo time.

$$\Delta\phi = 2\pi\gamma\, \Delta B\, TE \tag{2.21}$$

Based on the phase of the GRE image, the susceptibility of the brain can be calculated using equations 2.18 and 2.21 as demonstrated in the next section.

2.5 The Inverse Problem – Susceptibility from Phase

Shifts in susceptibility can be calculated from phase of a GRE image. As shown in Section 2.3, the field shift induced by an arbitrary susceptibility distribution is given by the convolution of the unit dipole point spread function with the susceptibility distribution. Since phase is linearly proportional to field shift, equation 2.21 can be rewritten as follows:

$$\Delta\phi(\vec{r}) = \gamma \cdot TE \cdot B_0\big(\chi(\vec{r}) * d(\vec{r})\big) \tag{2.22}$$

The calculation of the susceptibility distribution from the phase shift is an ill-posed, ill-conditioned inverse problem. The inverse problem can be solved either by writing the convolution in matrix form or in the frequency domain as a point by point division.

The convolution in equation 2.22 can be rewritten in matrix vector form according to the equation below, where $\Delta\hat{\phi}$ is the measured phase shifts as a column vector, C is a sparse,

Toeplitz matrix representing the convolution kernel $\gamma \cdot TE \cdot B_0 \cdot d(\vec{r})$, and $\hat{\chi}$ represents the susceptibility distribution as a column vector.

$$\Delta\hat{\phi} = C\hat{\chi} \tag{2.23}$$

Since this system of equations is ill-posed and ill-conditioned and the matrix *D* is very large for MR problems, direct inversion of the matrix *D* is usually impossible. A regularized solution is generally found using iterative methods. These formulations are described at length in Chapter 4.

Alternatively, the susceptibility can be calculated as a point by point division in the frequency domain as shown in equation 2.24 below where $\Delta\Phi$ is the measured phase shift in the frequency domain.

$$\mathrm{X}(\vec{k}) = \frac{\Delta\Phi(\vec{k})}{\gamma \cdot TE \cdot B_0 \cdot D(\vec{k})} \tag{2.24}$$

Recalling that $D(\vec{k}) = \left(\frac{1}{3} - \frac{k_z^2}{k^2}\right)$, a divide by zero occurs whenever $\frac{1}{3} = \frac{k_z^2}{k^2}$. The divide by zero results in amplification of noise and streaking artifacts. Typically, the divide by zero is removed by thresholding $D(\vec{k})$ to a minimum value. However, this approach results in a tradeoff between artifact reduction and computational accuracy. A new approach to computing the susceptibility in the frequency domain based on the Wiener deconvolution is described and validated in Chapter 4.

CHAPTER 3

REMOVAL OF FIELD INHOMOGENEITIES

3.1 Overview

The phase of the GRE images reflects magnetic field shifts not only from intrinsic tissue properties, but also external field effects due to inhomogeneities in the main field, B_0, and uneven RF excitation, B_1. The measured phase also wraps around every 2π according to equation 3.1 below.

$$\phi_{measured} = mod(\phi_{actual}, 2\pi) \tag{3.1}$$

Phase wrapping and the effect of magnetic field inhomogeneities can be seen as banding effects and wide-scale phase variations as seen in the axial phase image below.

Figure 3.1: Axial 3D GRE phase image, TE=11.7 ms, voxel size .6x.6x.6 mm^3 showing the effects of B_0 and B_1 inhomogeneities and 2π phase wraps obscuring relevant tissue contrasts

In order to accurately quantify tissue susceptibility, the phase image must be unwrapped, and the B_0 and B_1 inhomogeneities removed. Imperfect removal of external field can result in increased streaking artifacts, a loss of contrast, and inaccurate quantitative measurements in the susceptibility map.

Many methods have been developed for phase unwrapping and the removal of external field inhomogeneities. The most popular phase unwrapping methods rely on cost function optimization, fitting functions, filtering and region merging[6]. Methods for removing external field inhomogeneities include high pass filtering, polynomial fitting, and the projection of dipole fields to fit the measured field based on relevant boundary conditions. The most popular methods are described and compared in the following sections.

3.2 Phase Unwrapping

Phase unwrapping is often the first step in removing undesired magnetic field inhomogeneities before calculating tissue susceptibility. Since phase is bounded between 0 and 2π, wrapping occurs when the measured phase signal exceeds the boundaries. Unwrapping algorithms seek to recover the original smooth phase.

3.2.1 FSL PRELUDE

FSL's PRELUDE is a common technique used to unwrap MR data sets, and available as part of the FSL utilities (FMRIB Oxford)[6]. The PRELUDE algorithm relies on region merging based on a cost function. The cost function penalizes the phase differences along interfaces between phase regions. PRELUDE uses a sum of squared difference in phase as shown in equation 3.2 below.

$$C_{AB} = \sum_{j,k\epsilon N(j)} \left(\phi_{Aj} - \phi_{Bk} + 2\pi M_{AB}\right)^2 \quad (3.2)$$

C_{AB} represents the cost between regions A and B, ϕ_{Aj} and ϕ_{Bk} is the phase of the j[th] voxel in region A and the k[th] voxel in B respectively, and M_{AB} represents an integer defining the number of 2π wraps between the regions.

Phase unwrapping is conducted by choosing M_{AB} in order to minimize the cost over all the interfaces.

$$\min_{M_{AB}} \sum_{A,B} C_{AB} \quad (3.3)$$

The solution of equation 3.3 above can be found by setting the derivative of the cost function to zero:

$$M_{AB} = -\frac{P_{AB}}{2\pi N_{AB}} \quad (3.4)$$

where $P_{AB} = \sum_{j,k\epsilon N(j)} \left(\phi_{Aj} - \phi_{Bk}\right)$ and N_{AB} is the number of voxel pairs on the interface.

Since solving for equation 3.4 is difficult as M_{AB} is an integer, equation 3.4 can be rewritten as equation 3.5 below, which can be shown to have the same minimum as equation 3.4.

$$M_{AB} = round\left(\frac{-P_{AB}}{2\pi N_{AB}}\right) \quad (3.5)$$

PRELUDE divides the image into initial regions by selecting contiguous regions of phase within a certain interval and then merges the regions from the highest cost region to the lowest by using equation 3.5 above.

In high resolution GRE in vivo brain images as well as numerical phantoms data, PRELUDE provided very robust and accurate phase unwrapping up to an arbitrary 2π offset as shown in Figure 3.2 below.

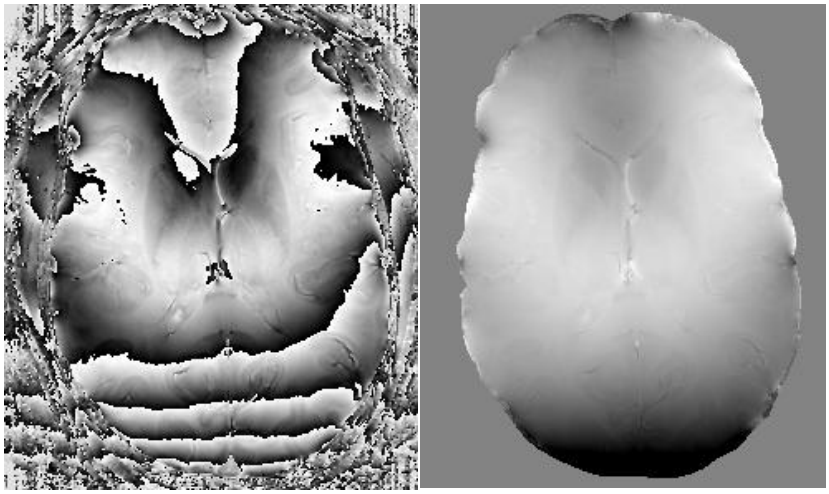

Figure 3.2: Slice of an axial phase image of the brain with wrapped phase (left) and PRELUDE unwrapped phase (right)

However, for large 4D in vivo data sets, PRELUDE ran very slowly taking approximately 48 hours to unwrap a 448x448x226x5 voxel data set. PRELUDE is generalized to provide unwrapping in both 3D and 2D. A great improvement in speed is provided by running PRELUDE in 2D, but it was found that unwrapping in 2D introduces errors in the through slice direction.

3.2.2 Gradient Matching

An alternative way of unwrapping phase data is to integrate the gradient of the wrapped images and then apply the offset lost in the integration by calculating unwrapped areas of phase based on linearity. A wrapped phase image should have an identical gradient compared to the original image except at the points where wraps occur. The location of the wraps can be shifted by applying a constant phase offset to the complex image. This allows accurate gradient data to be

acquired across in the entire image by applying a median filter to the set of gradients of the unwrapped phases. The median filter removes the erroneous outlier gradients caused by the 2π jumps in phase.

$$\nabla\phi_{unwrapped} = median\left\{\nabla\left(\phi_{wrapped} + \frac{n\pi}{N}\right)\right\}, for\ n = 1,2, \dots N \tag{3.6}$$

The original unwrapped phase can be recovered by integrating the gradient:

$$\phi_{unwrapped} = \iiint \nabla\phi_{unwrapped} dxdydz \tag{3.7}$$

This approach allows the unwrapped phase to be calculated very quickly, and this method is easily generalized for unwrapping in N-dimensions. However, any errors in the gradient calculation will propagate through the integration step resulting in artifacts in the image. This problem can be avoided by reformulating the integration as a least squares minimization:

$$\min_{\phi_{unwrapped}} |\nabla\phi_{unwrapped} - \nabla\phi_{wrapped}|_2^2 \tag{3.8}$$

The minimization problem can be solved by rewriting the cost function as a matrix vector equation and solving for the solution iteratively using conjugate gradients[7]:

$$\min_{\hat{\phi}_{unwrapped}} \left\| \begin{bmatrix} G_x \\ G_y \\ G_z \end{bmatrix} \hat{\phi}_{unwrapped} = \widehat{\nabla\varphi}_{unwrapped} \right\|_2^2 \tag{3.9}$$

where G_x,G_y, *and* G_z are matrices corresponding to gradient operations in the *x*,*y*, and *z* direction, $\hat{\phi}_{unwrapped}$ is a column vector of the unwrapped phase, and $\widehat{\nabla\varphi}_{unwrapped}$ is a column vector of the unwrapped phase gradient found in equation 3.6.

The gradient matching algorithm was tested using numerical and in vivo data. A 3D numerical phantom was generated and phase wraps were simulated whenever the phantom exceeded the range [-π,π]. The gradient of the numerical phantom was estimated by finding the median of the gradient of the wrapped data with offsets of 0, π/5, 2π/5, 3π/5, and 4π/5. Increments of π/5

offsets were chosen, because it shifted the wraps sufficiently to calculate accurate phase gradients. The conjugate gradients matching algorithm was used to unwrap the data set from the gradient information.

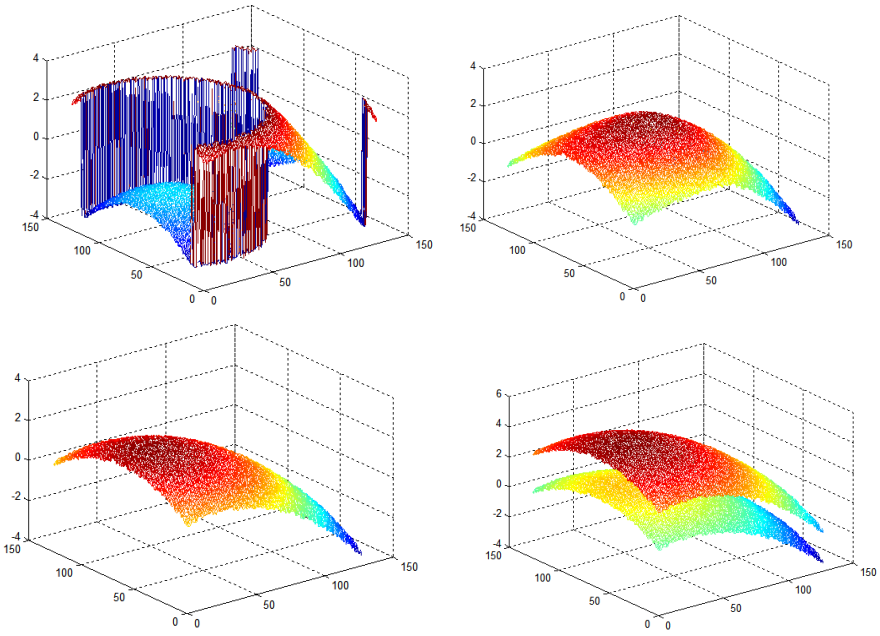

Figure 3.3: Top left: wrapped numerical phantom, Top right: output of conjugate gradients unwrapping after 100 iterations, Bottom left: Output of conjugate gradients after 200 iterations, Bottom right: Output of the unwrapping algorithm compared to the original phase demonstrating good unwrapping up to a global offset

As seen in Figure 3.3 above, the gradient matching algorithm was able to successfully unwrap the phase of the numerical phantom up to a constant offset after 200 iterations.

The algorithm was also tested on in vivo data as shown in Figure 3.4.

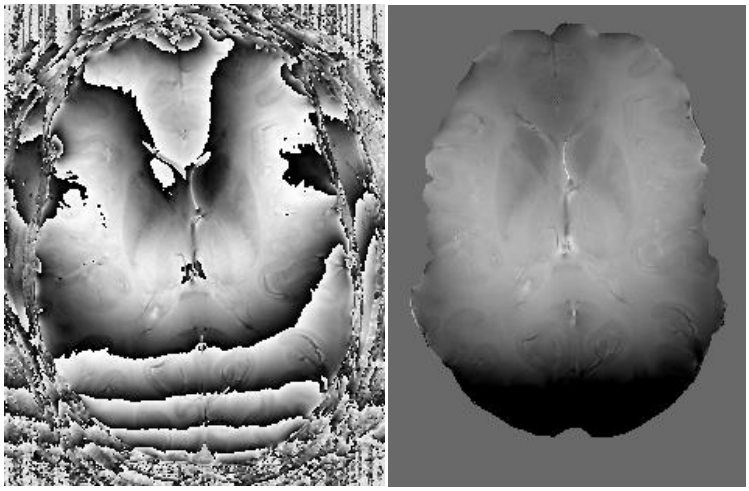

Figure 3.4: 336x336x236 axial brain image unwrapped using gradient matching

On larger and noiser in vivo data sets convergence was slower and less accurate than on the numerical phantom. Convergence can be greatly improved by applying appropriate preconditioners to raise the condition number of the matrix in equation 3.9. With improved convergence on in vivo data sets, gradient matching could prove to be a much faster alternative to FSL's PRELUDE.

3.3 B_1 and B_0 Field Removal

3.3.1 Homodyne High Pass Filter

High pass filtering is a popular approach for removing large scale phase variations due to B_0 and B_1 inhomogeneities[8]. This approach assumes that tissue susceptibility effects are local and exist primarily in high spatial frequencies, while external field effects exist primarily in the low spatial frequencies. If there is little to no overlap in their spectrum, then the tissue effects can be extracted as follows:

$$\phi_{tissue} = angle\left(FT^{-1}\left(H \cdot FT(I)\right)\right) \tag{3.10}$$

where *I* is the complex image, and *H* is a 3D transfer function representing a low pass filter. Since the homodyne filter works on complex data, phase unwrapping is not necessary for homodyne filtered phase images. This makes homodyne filtering a fast, efficient and easily implemenTable preprocessing method.

A 2-D homodyne filter of varying strengths was used to extract phase data from a five echo GRE complex image data with TE_0=3.1 ms and dTE=4.3 ms and isotropic .6 mm voxels. Static field effects were eliminated by complex division of echo 3 by echo 1 for an effective dTE of 8.6 ms. The complex data was then filtered using the Gaussian low pass filter shown below.

$$H(k_x, k_y) = e^{-\frac{\left(k_x - \frac{N_x}{2}\right)^2 + \left(k_y - \frac{N_y}{2}\right)^2}{2\sigma^2}} \tag{3.11}$$

In equation 3.11, N_i is the number of voxels in the i^{th} dimension and σ is a parameter which determines the strength of the high pass filter. The original complex data was then divided by the smoothed data resulting in a high pass filtered image. The results are shown in Figure 3.5 below.

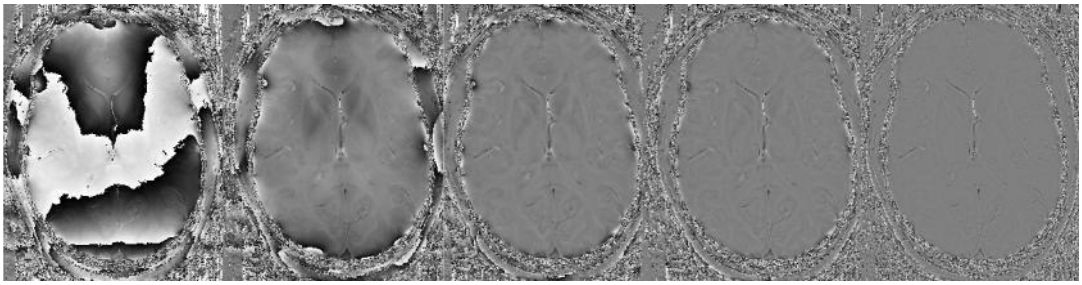

Figure 3.5: From left to right: unfiltered, σ=2.02, 6.05, 10.09, 20.18

As seen in Figure 3.5 above, homodyne high pass filtering is a tradeoff between tissue contrast and removal of external magnetic field inhomogeneities. As the strength of the filter is increased contrast between tissues is removed and only the edges of the image are retained. This is

especially noticeable and problematic for iron storing tissues such as the basal ganglia as seen in the enlargement below.

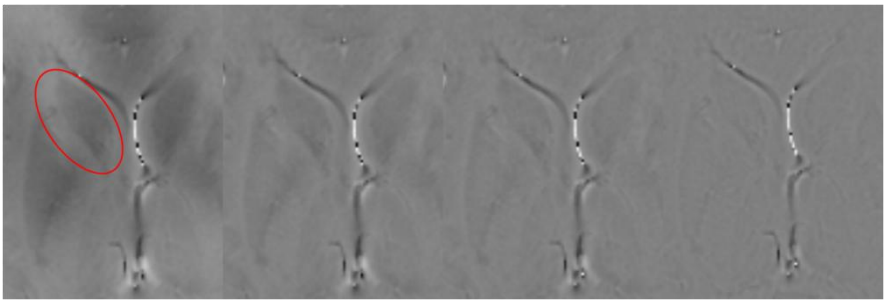

Figure 3.6: Detail of the basal ganglia demonstrating contrast loss between different tissues as filter strength increases

The ideal filter strength was σ= 6.05 for this example, judging by a qualitative tradeoff between image flattening and contrast retention. However, this filter strength is dependent on the TE, and the quality of the data. Longer TE's and poor shimming requires stronger filters and result in higher contrast losses.

3.3.2 Polynomial Fitting

Polynomial fitting of the unwrapped phase is an alternative method for estimating slowly varying external field contributions. A least squares polynomial fit can be formulated as a system of equations as shown below:

$$V\hat{p} = \hat{\phi} \tag{3.12}$$

where V is a matrix whose column vectors are the terms of the polynomial ie: x^n, x^{n-1}…, $\hat{p}$ is a column vector containing the coefficients of the polynomial, and $\hat{\phi}$ is the image rewritten as a column vector. Since the system of equations is overdetermined for MR applications, the least squares solution for the polynomial coefficients is solved by applying the Moore-Penrose pseudoinverse as shown below.

$$\hat{p} = (V^T V)^{-1} V^T \hat{\phi} \tag{3.13}$$

A 5th order polynomial was used to estimate the external field effects on a 2D slice of an unwrapped GRE phase image with TE=11.7 ms and isotropic .6mm voxels as shown below. Since $V^T V$ becomes ill-conditioned for high order polynomials, there was very little gain in using polynomial fits of a higher order.

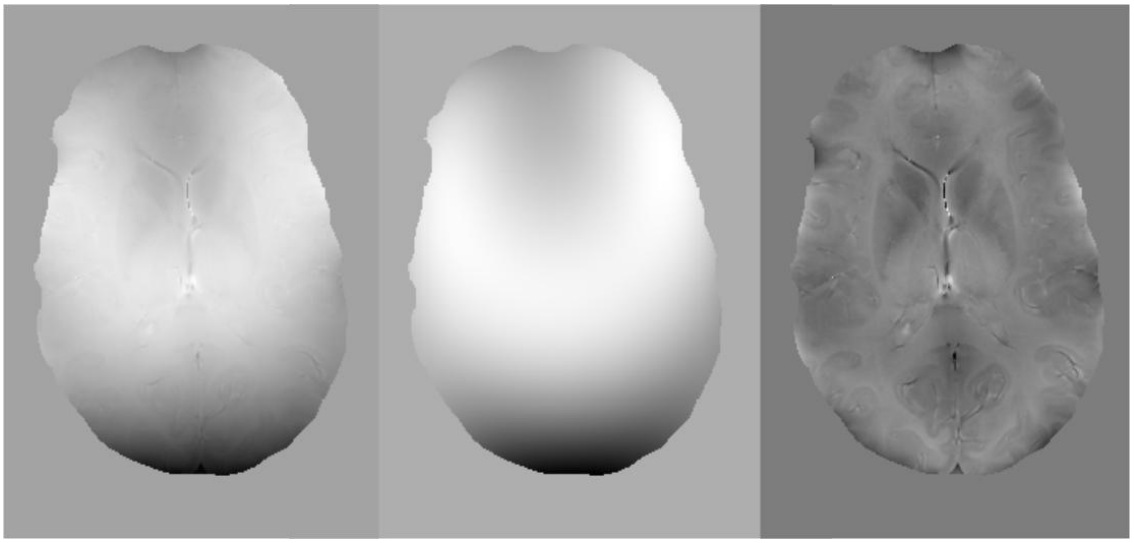

Figure 3.7: Left to right: Unwrapped phase image, 5th order polynomial approximation of external field, corrected phase

As seen in Figure 3.7 above, a 2D polynomial fit does a good job of retaining image contrast compared to high pass filtering. However, the corrected image retains some large scale variation that is inconsistent with actual tissue susceptibilities.

3.3.3 Short TE Phase Scaling

The primary drawback to high pass filtering is that it significantly reduces tissue contrasts due to spectral overlap between the field caused by intrinsic tissue properties and the external field. High pass filtering assumes that the external field effects are slowly varying across the image,

and are thus constrained to lower spatial frequencies, while the intrinsic field effects are local and thus confined to the higher spatial frequencies. In practice, this assumption does not hold, especially in large iron storing structures such as the basal ganglia. The loss of contrast and inaccuracies caused by the use of high pass filter was demonstrated in Section 3.3.1.

A novel method of estimating the external field effects was developed and tested using additional data acquired using fast low resolution scans with extremely short echo spacing. This method assumes that the phase of the image is comprised of a spatially varying offset, ϕ_1, primarily caused by RF phase, and an echo time dependent component, $\phi_0(TE)$, due to main field inhomogeneities and tissue susceptibility.

$$\phi = \phi_0(TE) + \phi_{tissue}(TE) + \phi_1 \tag{3.14}$$

Since $\phi_1$is constant over time, its effect is removed by subtracting two echoes at different TE's.

$$\phi_{TE2} - \phi_{TE1} = \phi_0(TE2 - TE1) + \phi_{tissue}(TE2 - TE1) \tag{3.15}$$

By choosing an extremely short *dTE=TE2-TE1*, phase wraps can also be eliminated. As TE is short, the contrast due to ϕ_{tissue}effects is also limited allowing a thresholded moving average filter to remove localized effects due to ϕ_{tissue}.

$$\phi_0 = \frac{LPF\{\phi_{TE2} - \phi_{TE1}\}}{TE2 - TE1} \tag{3.16}$$

Using the estimated ϕ_0, the phase inhomogeneities due to main magnetic field inhomogeneities can be removed by scaling the estimated field by TE and subtracting it from the target image.

The short TE phase scaling approach was applied to a sagittal GRE brain image. The field map was estimated using two low resolution scans with TE 1.55 ms and 1.34 ms respectively using

the procedure described above. A 16x16x16 thresholded moving average filter was used to smooth the difference between $\phi_{TE1.55}$ and $\phi_{TE1.34}$ to estimate ϕ_0. The resulting field map was interpolated to .5x.5.x5 mm voxels and used to estimate and remove the external field from a .5x.5.x.5mm GRE image with *dTE*=15ms. The time invariant phase in the high resolution image was removed prior to removing the B_0 field by complex division of echo 1 and 3. The results are shown in Figure 3.8 below.

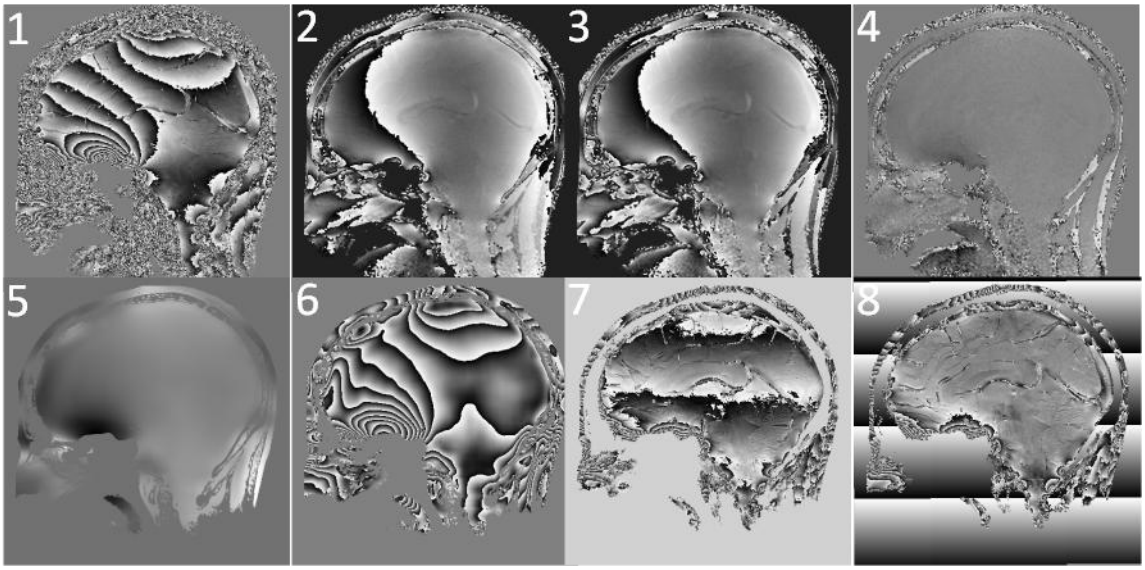

Figure 3.8: 1: Phase difference image between echo 1 and echo 3 calculated by complex division from high resolution SWI dTE=15 ms, 2: Phase image from low resolution scan TE=1.55 ms, 3: Phase image from low resolution scan TE=1.34 ms, 4: Phase from subtraction by complex division of the low resolution scans with dTE=.21 ms 5: Estimate of B_0 6: Estimate of phase inhomogeneity at dTE=15ms from B_0 7: Corrected high resolution phase showing linear phase shift 8: Final corrected phase

As seen in Figure 3.8, the estimated B_0 map in this example was successful at estimating the field inhomogeneities in the high resolution scan except for a linear gradient. This linear gradient represents a *k*-space offset between the high resolution scan and low resolution correction scan, and can be easily removed as seen in the final result below.

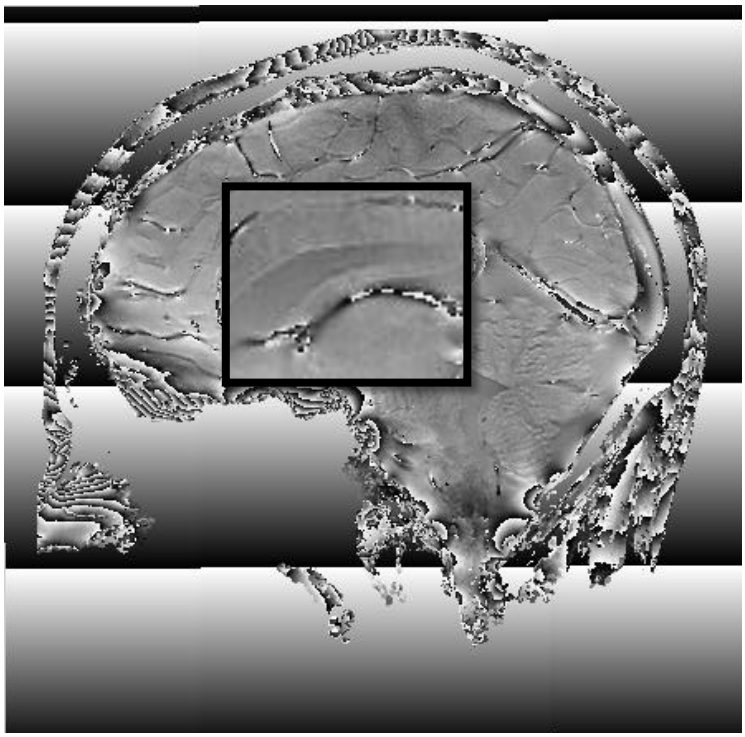

Figure 3.9: Final corrected brain with magnification showing that phase contrast is well preserved in the area around the basal ganglia

As seen in Figure 3.9 above, removes magnetic field inhomogeneities without eliminating tissue contrasts. The method also does a good job of preserving image quality to the edges of the brain. Error in the B_0 estimation was primarily limited to veins and arteries where the phase had multiple wraps in each voxel and could not be recovered.

Although results in this example were very promising, short TE phase scaling was not found to provide good B_0 estimates in the majority of in vivo cases, and the corrected images contained additional phase inhomogeneities. Recently high resolution in vivo GRE images were demonstrated to have an echo dependent *k*-space offset. This would present itself as a linear shift in phase and has not been accounted for by the algorithm in its present form. Also, at high fields, eddy currents and pulsations in the cerebrospinal fluid and other effects may also play

significant role. Hopefully, by updating the algorithm to account for these effects, this algorithm would prove successful on a greater number of data sets.

3.3.4 Projection on Dipole Fields

A non-parameterized model was recently developed by Liu et al, which relies on the orthogonality of field perturbations originating from susceptibility effects within the brain with the field perturbations caused by external effects such as main field inhomogeneities and tissue air interfaces[9]. Since the internal and external field effects are orthogonal, the external field effects can be estimated by simulating a susceptibility distribution outside of the brain without removing field effects due to tissue susceptibility within the brain. This can be formulated as the minimization problem in quadratic form as shown in equation 3.17 below.

$$\min_{\hat{\chi}} \left| W\left(C\hat{\chi} - \Delta\hat{B}\right) + \alpha(1 - W)\hat{\chi} \right|_2^2 \tag{3.17}$$

In equation 3.17, W is a diagonal matrix representing a mask with ones on the inside of the brain and zeros outside, C is a Toeplitz matrix representing the convolution in equation 2.19, $\Delta\hat{B}$ is the measured field shifts, and α is a constant which controls the relative strength of each term. For large α, the solution to 3.17 finds a collection of dipoles outside of the brain which best approximates the external field effects within the brain. Since the image volume contains more than 2.6×10^7 data points, storage of the matrix, C, in equation 3.17 is impossible. Instead, the convolution operation was conducted using the frequency domain approximation derived in Section 2.3.

The minimization problem in equation 3.17 was solved iteratively using conjugate gradients, which minimizes *Ax*-*b*. For equation 3.17, *A* and *b* can be defined as follows by expanding equation 3.17:

$$A = C^T W^T W C + \alpha^2 (1 - W)^T (1 - W) \tag{3.19}$$

$$b = 2C^T W^T W \Delta\hat{B} \tag{3.20}$$

In order to calculate the internal field effects due to tissue susceptibility, the estimated external field was subtracted from the measured field shifts.

$$\Delta B_{int} = \Delta B - FT^{-1}(D(\vec{k}) \cdot \mathrm{FT}(\chi)) \tag{3.21}$$

The algorithm was used to estimate the external field of a GRE phase image. The image was acquired at 7T with TE1=3.1 ms and echo spacing dTE=4.3 ms, isotropic .6 mm voxels, and an image matrix of 336x336x236. The static field effects were first removed by complex division of echo 3 by echo 1 for an effective TE of 8.6 ms. The results of the algorithm including several intermediate steps are shown in Figure 3.10 below.

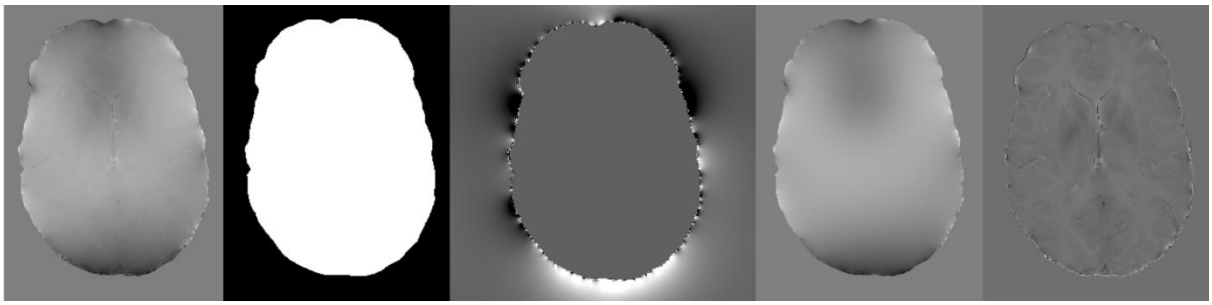

Figure 3.10: Left to right: ΔB, mask described by *W*, projected dipoles, estimated field,ΔB_{ext}, corrected field shifts, ΔB_{int}

The results of the PDF algorithm for two different slices in the image volume are depicted below.

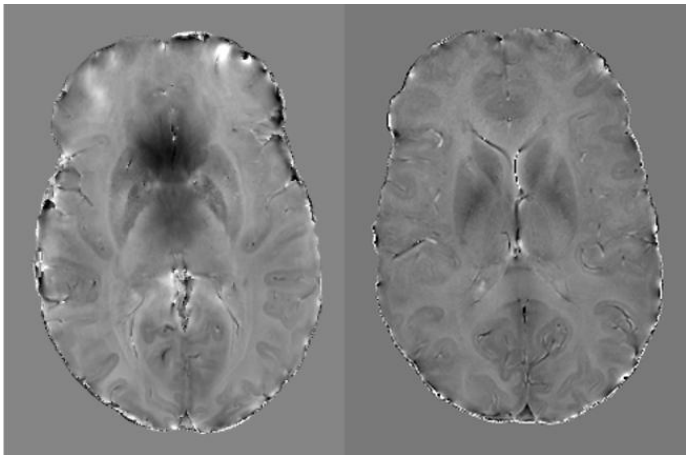

Figure 3.11: A comparison of two different slices from the same axial image volume corrected using PDF.

As seen in Figure 3.11, the correction works well for most areas of the brain and retains good tissue contrast in the basal ganglia and between white matter and grey matter. However, as seen in the image on the left, the algorithm gives poor correction close to tissue air interfaces.

3.3.5 Performance and Evaluation

The performance of homodyne high pass filtering, polynomial fitting, and projection on dipole fields was analyzed and compared. Short TE scaling has been excluded from the comparison, because modifications to the algorithm are necessary e.g. correction of *k*-space shifts between echoes. The performance of the algorithm was judged by how well it flattens the background field, while retaining tissue contrasts. Since similar tissues are expected to induce similar field shifts, variance in estimated field shifts between similar tissues from different parts of the brain would indicate incomplete removal of the background field. The ability of the algorithm to

preserve tissue contrasts was measured by calculating the contrast between the basal ganglia and the surrounding tissue as well as the contrast between the grey and white matter.

A 5 echo GRE complex image set was acquired at 7T (Philips) with TE_0=3.1 ms and dTE=4.3 ms. The data were acquired with isotropic .6mm voxels and an image matrix of 336x336x237 voxels. The static field effects were removed first by complex division of echo 3 by echo 1 for an image with a TE of 8.6 ms. The resulting phase image was processed using homodyne high pass filtering, polynomial fitting, and projection on dipole fields in order to generate field maps (field and phase are related according to equation 2.21). The resulting field maps in μT from each algorithm are shown in Figure 3.12 below.

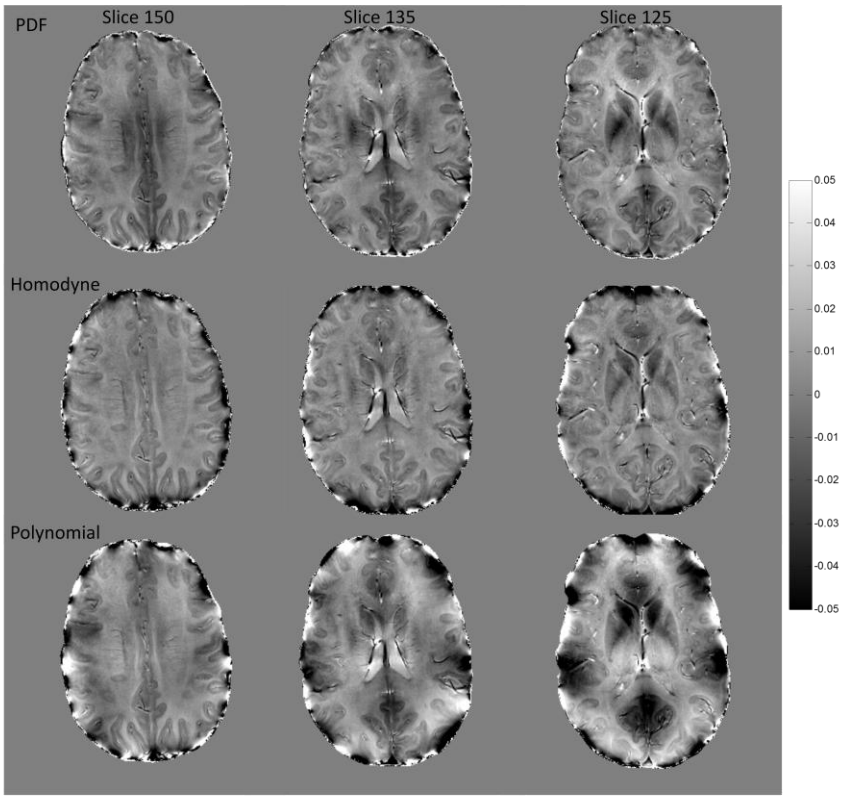

Figure 3.12: Field shifts induced by tissue susceptibility calculated by projection onto dipole fields (top), homodyne complex high pass filtering (middle), and polynomial fitting (bottom) shown for three different slices in the image volume

The brain was divided into four quadrants, and ROI's of the basal ganglia, white matter, and grey matter were drawn in each quadrant on three different slices using the magnitude image as a guide as shown in Figure 3.13 below. Additionally, ROIs were drawn in the basal ganglia in slice 135 and 125.

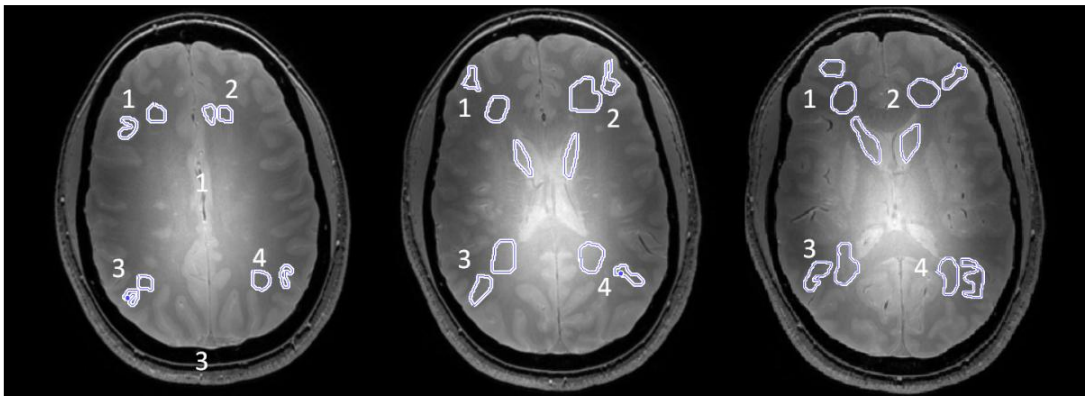

Figure 3.13: ROI's drawn on the brain in order to analyze how well each algorithm preserves contrast while removing external field effects

The mean and variance within each ROI shown in Figure 3.13 was calculated and tabulated below.

Table 3.1: Slice 150 field shift in each ROI in μT

	PDF		**Polynomial**		**Homodyne (σ=6.05)**	
	Mean	Variance	Mean	Variance	Mean	Variance
WM1	0.0061	1.24E-05	0.0103	1.11E-05	1.64E-04	1.07E-05
WM2	0.0066	7.36E-06	0.0116	6.08E-06	0.0031	7.39E-06
WM3	0.0014	6.37E-06	-0.0078	7.78E-06	0.0041	6.88E-06
WM4	0.0015	7.34E-06	0.0076	8.22E-06	0.0043	4.65E-06
GM1	-0.0077	9.06E-05	-0.0091	9.71E-05	-0.0047	9.50E-05
GM2	-0.0064	1.56E-05	-0.0073	1.80E-05	-0.0062	1.51E-05
GM3	-0.009	3.51E-05	-0.0192	6.37E-05	-0.0035	3.56E-05
GM4	-0.0113	3.78E-05	0.0012	3.94E-05	-0.0022	3.69E-05

Table 3.2: Slice 125 field shift in each ROI in μT

	PDF		Polynomial		Homodyne	
	Mean	Variance	Mean	Variance	Mean	Variance
WM1	0.0105	2.26E-05	0.0023	2.38E-05	0.0023	1.50E-05
WM2	0.0068	1.88E-05	0.0187	2.58E-05	0.0046	1.49E-05
WM3	0.0026	1.43E-05	0.0053	2.70E-05	0.0036	1.27E-05
WM4	0.0023	1.00E-05	0.0024	1.82E-05	0.0048	1.05E-05
GM1	-0.0079	5.09E-05	0.0055	8.14E-05	-0.0011	3.69E-05
GM2	-0.0178	8.13E-05	-0.0296	1.51E-04	-0.0059	1.10E-04
GM3	-0.0066	2.08E-05	-0.0014	3.06E-05	-0.0013	2.63E-05
GM4	-0.009	1.28E-05	0.0188	3.76E-05	-0.0026	1.44E-05
BG1	-0.0113	2.68E-05	-0.0127	8.28E-05	-0.0076	3.74E-05
BG2	-0.0144	3.66E-05	-0.0091	5.19E-05	-0.0102	3.86E-05

Table 3.3: Table 2: Slice 135 field shift in each ROI in μT

	PDF		Polynomial		Homodyne	
	Mean	Variance	Mean	Variance	Mean	Variance
WM1	0.019	1.28E-05	0.0146	2.72E-05	0.0037	2.12E-05
WM2	0.0143	1.76E-05	0.0216	3.94E-05	0.0028	1.87E-05
WM3	0.0066	2.06E-05	0.0044	3.67E-05	0.002	1.97E-05
WM4	0.0074	5.58E-06	0.012	3.30E-05	0.0042	5.91E-06
GM1	0.0018	4.34E-05	-0.0053	1.59E-04	5.71E-04	3.37E-05
GM2	-0.0037	1.23E-04	-0.0243	4.35E-04	-0.0028	2.43E-04
GM3	-0.0037	2.90E-05	0.0051	1.52E-04	-0.0038	3.61E-05
GM4	-0.0049	7.47E-05	0.0144	1.08E-04	-0.0053	7.17E-05
BG1	-0.008	2.35E-04	-0.0393	3.04E-04	-0.0184	9.10E-05
BG2	-0.013	1.12E-04	-0.0375	7.74E-05	-0.0207	4.06E-05

The coefficient of variability, the ratio between the mean and the standard deviation, was calculated from the set of mean field shifts from Tables 3.1-3. This is a measure of how well the algorithm removes the external field as similar tissues should have similar field shifts across the brain. Lower values indicate better performance.

Table 3.4: Standard deviation to mean ratio of white matter and grey matter for each algorithm

		Mean (μT)	Standard Deviation to Mean Ratio
GM	PDF	-.0072	.66
	Polynomial	-.0043	3.46
	Homodyne	-.0032	.64
WM	PDF	.0071	.75
	Polynomial	.0086	.93
	Homodyne	.0033	.40

As seen in Table 3.4, homodyne high pass filtering maintained the greatest homogeneity within similar tissue types, while polynomial fitting performed the worst. This is consistent with a qualitative comparison of Figure 3.12 above.

Next the ability of each algorithm to maintain tissue contrasts was analyzed. Contrast between white matter/grey matter and white matter/basal ganglia within each quadrant was calculated using equation 3.22 below where I_x denotes the intensity of the tissue of type x.

$$Contrast = \frac{\sqrt{I_1^2 - I_2^2}}{\sqrt{I_1^2 + I_2^2}} \tag{3.22}$$

The ability of each algorithm to maintain white matter/grey matter and white matter/basal ganglia contrast was calculated and tabulated below.

Table 3.5: Average contrast between white matter and grey matter and white matter and basal ganglia for each algorithm

	Avg. Contrast WM/GM	Avg. Contrast BG/WM
PDF	1.26	1.37
Polynomial	.925	1.29
Homodyne	1.29	1.22

As seen in Table 3.5 above, PDF and homodyne high pass filtering performed similarly for preserving white and grey matter contrast, while polynomial fitting performed comparatively poorly. PDF outperformed both polynomial fitting and homodyne high pass filtering for preserving basal ganglia contrast. The decline in the performance of high pass filtering is expected, because the basal ganglia is a much larger and more homogeneous structure compared to the gyri, and is therefore more affected by high pass filtering. The quantitative analysis is consistent with the visual performance of the algorithms as shown in Figure 3.12 above.

Homodyne high pass filtering and PDF clearly outperformed polynomial fitting in terms of background field removal and contrast preservation. While homodyne high pass filtering and PDF preserved similar levels of contrast between white matter and grey matter, PDF clearly outperformed homodyne high pass filtering in larger structures such as the basal ganglia. As shown in Table 4 above, there was also a loss in energy in the high pass filtered image compared to either PDF or polynomial fitting. PDF was found to be the most proficient background field removal algorithm for quantitative susceptibility mapping.

CHAPTER 4

QUANTITATIVE SUSCEPTIBILITY MAPPING

4.1 Overview

Calculating susceptibility maps from field shifts is a non-trivial problem. Although the mathematical formulation is a straightforward point by point division in the frequency domain, the presence of zeros in the transfer function, $D(\vec{k}) = \left(\frac{1}{3} - \frac{k_z^2}{k^2}\right)$, creates substantial problems in the inversion.

$$\mathrm{X}(\vec{k}) = \frac{\Delta\Phi(\vec{k})}{\gamma \cdot TE \cdot B_0 \cdot D(\vec{k})} \tag{4.1}$$

Zeros in the denominator occur in a conical region whenever $\frac{1}{3} = \frac{k_z^2}{k^2}$ as shown in Figure 4.1 below.

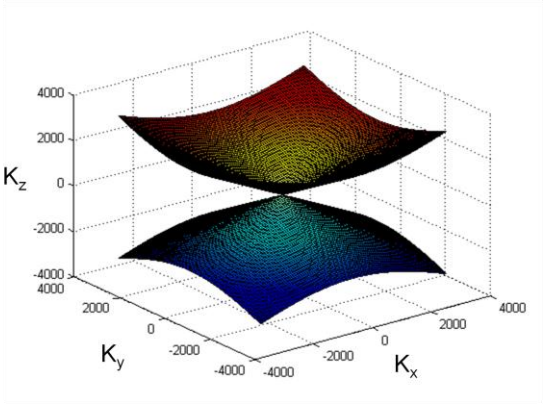

Figure 4.1: $\frac{1}{3} \approx \frac{k_z^2}{k^2}$ defines a cone in *k*-space

The resulting divide by zero amplifies noise in the spatial frequencies defined by the cone and results in streaking artifacts in the reconstructed image. As seen in the image example below, streaking artifacts can greatly hinder the quantitative accuracy and comprehensibility of the reconstructed image.

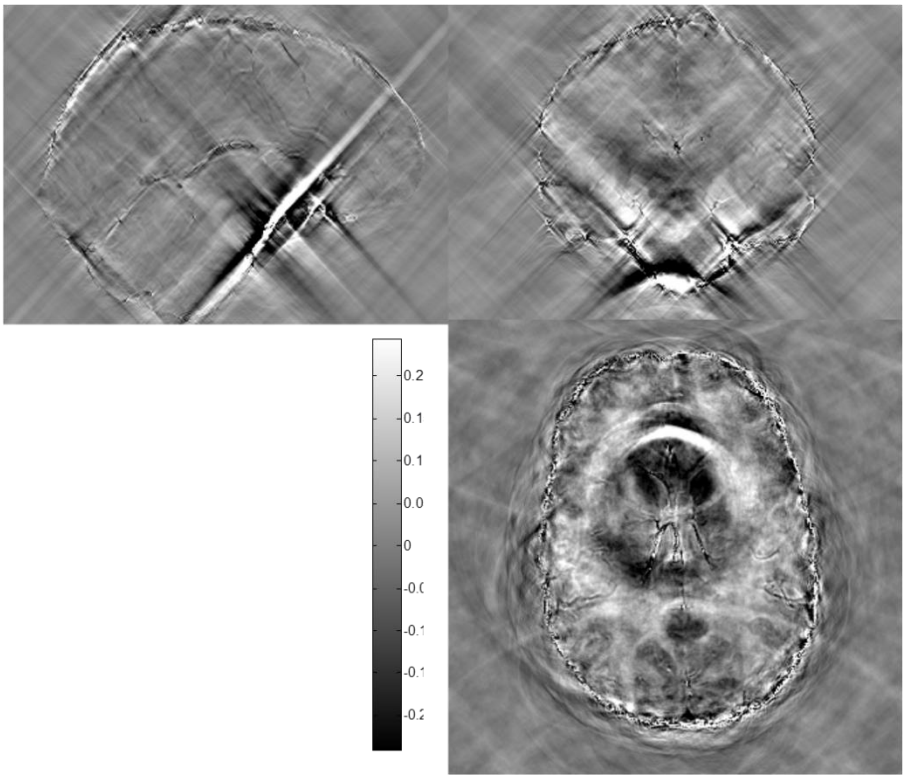

Figure 4.2: Streaking artifacts caused by the divide by zero in *k*-space

Due to the divide by zero, the inversion problem from field shift to susceptibility is ill-posed and requires careful conditioning to avoid reconstruction artifacts.

Algorithms have been developed to address the streaking artifacts with varying levels of success. Current methods include acquiring data with the object at a variety of orientations in regards to the magnetic field in order to fill in the missing data in *k*-space[10], image domain regularization techniques[11], and thresholding of the transfer function[12][13]. The algorithms are described in depth in Section 4.2 along with a novel method of regularizing the transfer function in the frequency domain. In section 4.3, the performance of the single orientation methods is tested and compared using numerical phantoms, MR phantoms, and in vivo data.

4.2 Algorithms

4.2.1 Multiple Orientations

An effective method for stabilizing the inversion problem is to acquire data with the object at multiple orientations with respect to the main magnetic field. Because the transfer function, $D(\vec{k})$, is rotationally dependent, the location of the zeros in *k*-space is rotated depending on the orientation of the object within the field. By acquiring images at multiple orientations, accurate calculations can be made for the entirety of *k*-space.

The rotational dependency of $D(\vec{k})$ can be described for a rotation, θ, about the *x*-axis and ϕ about the *y*-axis as follows:

$$D(\vec{k},\theta,\phi) = \left(\frac{1}{3} - \frac{(k_z cos\theta cos\phi - k_y sin\theta sin\phi + k_x sin\phi)^2}{k^2}\right) \tag{4.2}$$

The susceptibility can be calculated from the multiple orientation data by choosing the solution $\chi(\vec{k})$ which best satisfies:

$$\begin{bmatrix} D_1 \\ D_2 \\ \dots \\ D_N \end{bmatrix} \chi(\vec{k}) = \begin{bmatrix} \Delta B_z^1(\vec{k}) \\ \Delta B_z^2(\vec{k}) \\ \dots \\ \Delta B_z^N(\vec{k}) \end{bmatrix} \tag{4.3}$$

where D_n is the transfer function describing the n^{th} orientation, and $\Delta B_z^n(\vec{k})$ is the field shifts observed for the n^{th} orientation.

4.2.2 Single Orientation Thresholding

Because acquiring multiple acquisitions at multiple orientations can be time consuming and uncomforTable for the patient, single acquisition techniques are preferred for diagnostic scans. The most primitive manner of dealing with the zero divide is to threshold the transfer function such that values less than a threshold, t¸are set equal to t.

$$D'(\vec{k}) = \begin{cases} D(\vec{k}) & \text{for } |D(\vec{k})| \leq \text{t} \\ \text{t} & \text{for } D(\vec{k}) > t \\ -\text{t} & \text{for } D(\vec{k}) < -\text{t} \end{cases} \tag{4.4}$$

Although this method removes the divide by zero, relatively large values of t are necessary to avoid streaking artifacts. Using large values of t, the accuracy of the reconstruction is expected to suffer as less of the original transfer function is retained.

The susceptibility can be computed using the thresholded transfer function, $D'^{(\vec{k})}$:

$$\text{X}(\vec{k}) = \frac{\eta \Delta\Phi(\vec{k})}{\gamma \cdot TE \cdot B_0 \cdot D\prime(\vec{k})} \tag{4.5}$$

In equation 4.5, $\eta = \sqrt{E\{|D/D'|^2\}}^{-1}$ is a scalar which compensates for energy lost in the thresholding operation performed by equation 4.5. Here $E\{\}$ denotes the expectation operator.

4.2.3 Single Orientation Spatial Domain Regularization

An alternative regularization strategy is to apply spatial priors as constraints to the inversion problem. A reasonable regularization strategy is to enforce zero susceptibility outside of the brain and to specify the location of edges in the susceptibility distribution based on *a priori* knowledge of the structure of the brain. Applying these constraints, the matrix-vector formulation of the convolution between the unit dipole and an arbitrary susceptibility distribution becomes:

$$\min_{\hat{\chi}}\left(\left|W_1\left(C\hat{\chi}-\Delta\hat{B}\right)\right|_2^2+\alpha^2|M\hat{\chi}|_2^2+\beta^2|W_0G\hat{\chi}|_2^2\right) \tag{4.6}$$

where C is a Toeplitz matrix that describes the convolution kernel in the spatial domain, $\hat{\chi}$ is a column vector describing the tissue susceptibility, $\Delta\hat{B}$ is a column vector of measured field shifts, and G is the gradient matrix. W_1 is a matrix which weights the error in the image based on SNR. Since the noise in the phase image is inversely proportional to the magnitude image, a normalized magnitude image is a good choice for W_1. M is a diagonal matrix which represents a mask with ones outside the brain and zeros inside the brain. W_0 is a diagonal matrix describing smoothness constraints on the susceptibility distribution. An appropriate choice of W_0 is the inverse of the gradient of the magnitude image. α and β are scalars which control the relative strength of the regularization terms.

Since the matrices become prohibitively large for MR data sets, the matrices C and G are not formed explicitly. The convolution operation described by C was conducted using a point by point multiplication by $D\left(\vec{k}\right)$ in the frequency domain, and the gradient operation was conducted by a convolution by [-1,1] in the spatial domain.

Since equation 4.6 is quadratic, the solution to equation 4.6 is equivalent to solving an equation of the form $\min_x Ax - b$, where:

$$A = 2(C^T W^T W C + \alpha^2 M^T M + \beta^2 G^T W_1^T W_1 G) \quad (4.7)$$

$$b = 2C^T W^T W \Delta\hat{B} \quad (4.8)$$

The solution to the minimization problem presented by equations 4.7 and 4.8 can be calculated iteratively using conjugate gradients.

4.2.4 Single Orientation by Transfer Function Filtering

Although the regularized solution described in Section 4.2.3 has been demonstrated to give accurate estimates of tissue susceptibility, its reliance on *a priori* information imposes smoothness constraints on the quantitative susceptibility map which may obscure useful information. Since $\beta^2|W_0 G\hat{\chi}|_2^2$ penalizes gradients which do not correspond to edges in the magnitude image, it is equivalent to imposing a piece wise constant constraint on the reconstruction. This may introduce smoothing artifacts which obscure the fine structures around the periphery of lesions which are important for the study of inflammation in the MS process.

To address these concerns, a novel method for filtering the transfer function was developed based on the Wiener deconvolution[14]. The Wiener deconvolution uses *a priori* knowledge of the noise properties of the image to reduce artifacts introduced by the zero divide. The Wiener deconvolution applies a filter to the transfer function, $D(\vec{k})$, in *k*-space attenuating frequencies with low signal to noise ratio (SNR). The equation for the Wiener filter is shown below, where $G(\vec{k})$ denotes the filtered transfer function of the system, $D(\vec{k})$ denotes the transfer function,

and *S* denotes the strength of the filtering function in equation 4.9. The effect of the filtering operation decreases with *S*.

$$G(\vec{k}) = \frac{1}{D(\vec{k})}\left[\frac{|D(\vec{k})|^2}{|D(\vec{k})|^2+\frac{1}{S(\vec{k})}}\right] \tag{4.9}$$

The Wiener transfer function selectively attenuates regions of $D(\vec{k})$ in which noise is amplified. A good choice of *S* provides a better estimation of the susceptibility distribution with fewer artifacts compared to straight truncation or other established methods. An easy and effective choice of *S* is to choose a constant across all frequencies. Replacing $1/D(\vec{k})$ with the filtered version $G(\vec{k})$ in equation 4.1 allows fast estimation of the susceptibility distribution in the Fourier domain.

$$\mathrm{X}(\vec{k}) = \frac{\eta\Delta\Phi(\vec{k})\cdot G(\vec{k})}{\gamma\cdot TE\cdot B_0} \tag{4.10}$$

In equation 4.10, $\eta = \sqrt{E\{|D\cdot G|^2\}}^{-1}$ is a scalar which compensates for energy lost in the filtering performed by equation 4.9. Here, $E\{\}$ denotes the expectation operator.

4.3 Performance and Comparison

4.3.1 Methods

Numerical Phantom

The single orientation QSM methods were tested using numerical phantoms, MR phantoms, and in vivo data. Closed form solutions exist for the field perturbations caused by susceptibility distributions of simple geometries such as spheres and cylinders. The field perturbation caused by a sphere of radius, R_0, with susceptibility χ_i inside and χ_e outside inside a magnetic field B_0 in the *z*-direction induces a field shift ΔB_z:

$$\Delta B_z = \begin{cases} \frac{\chi_i - \chi_e}{3+\chi_e}\left(\frac{R_0}{r}\right)^3 (3\cos^2\theta - 1)B_0 & for\ r > R_0 \\ 0 & for\ r < R_0 \end{cases} \quad (4.11)$$

A numerical phantom was created of the field shift induced by a sphere with $R_0 = 3\ cm, \chi_i = .5\ ppm, \chi_e = 0\ ppm,$ and residing in a magnetic field, $B_0 = 7T$.

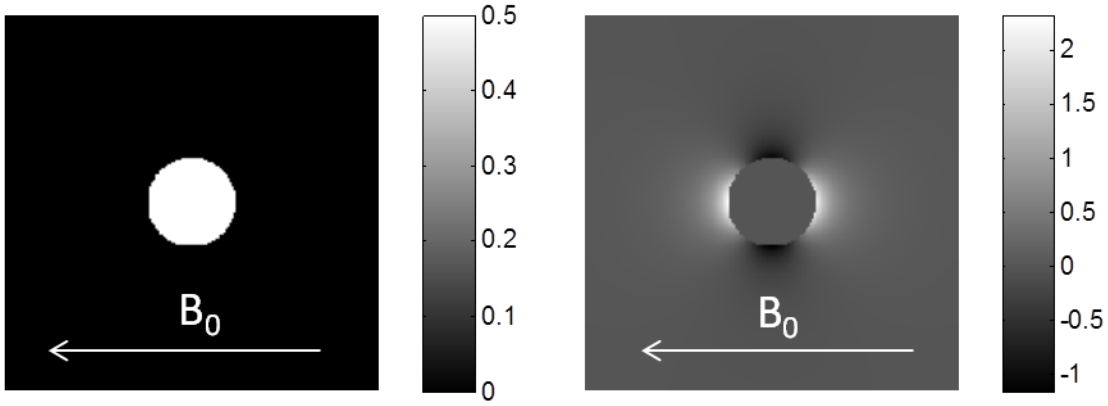

Figure 4.3: Left: a sagittal slice of the susceptibility distribution in ppm used to generate the numerical phantom, Right: a sagittal slice of the numerical phantom showing the field distortions in μT caused by a sphere

The numerical phantom was constructed with isotropic 1mm voxels and a 256x256x256 voxel image matrix.

The susceptibility was calculated using each of the single orientation methods described above. The parameters controlling the strength of each strategy was varied in order to observe the effect of the threshold value, the filter strength, and the regularization terms on the reconstructed image. The second regularization term was excluded from the spatial domain regularized method since the measured field shifts extended across the entire field of view. The calculated susceptibility was examined for image artifacts, and the numerical accuracy was computed by comparison to the known distribution.

MR Phantoms

Three MR phantoms with known susceptibilities were constructed as shown in Figure 4.4 below. Cylindrical containers with a length of 16 cm and a diameter of 9 cm were filled with a 4.5 g/L solution of NaCl.

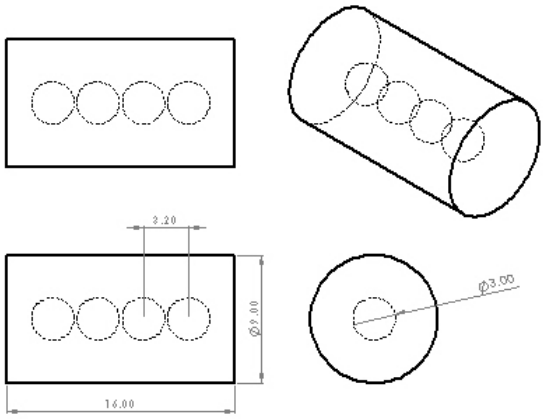

Figure 4.4: The design of the MR phantom

Balloons were used to construct four spherical compartments within the cylinder. The cylindrical shape of the phantom and the use of balloons minimized the amount of artifacts in the image due to uneven RF excitation and null signals at the boundaries between components.

The susceptibility within balloons was changed by varying the concentration of gadolinium (Magnevist). The gadolinium increases the local susceptibility by 326 ppm/M at 293 K. The susceptibilities used in the three phantoms are shown in Table 4.1 below.

Table 4.1: Susceptibilities of the balloons used in the three MR phantoms

	[Gd] (mM)	Susceptibility (ppm)
Phantom 1	.61	.20
	1.44	.47
	2.70	.88
	6.32	2.06
Phantom 2	1.53	.5
	3.19	1.04
	4.51	1.47
	6.13	2.00
Phantom 3	.15	.05
	.31	.10
	.92	.30
	1.23	.4

The phantoms were scanned on a Philips 7T scanner using a two echo GRE pulse sequence with TE1=1.54 ms and TE2=2.8 ms, isotropic .75mm voxels, and a 240x240x160 image matrix. The external field inhomogeneity was removed using the PDF algorithm described in Section 3.3.4. An extra masking step was used before PDF in order to mask unreliably unwrapped voxels near the periphery of the cylinder. The calculated field shifts were then used to generate quantitative susceptibility maps using each of the single orientation methods described in Section 4.2.

In Vivo Acquisition

A 5 echo GRE complex image set was acquired of a volunteer MS patient with IRB approval at 7T (Philips) with TE_0=3.1 ms and dTE=4.3 ms. The data were acquired with isotropic .6mm voxels and an image matrix of 336x336x237 voxels. The static field effects were removed first by complex division of echo 3 by echo 1 for an image with a TE difference of 8.6 ms. The resulting phase image was unwrapped using PRELUDE and processed using projection on dipole fields in order to generate field maps of the internal field perturbations in μT. The resulting field

maps were masked in order to remove unreliable voxels. Susceptibility maps were generated using each of the single acquisition algorithm described in the previous section, and the results were compared for the algorithm's ability to delineate different tissues and their depiction of MS lesions.

4.3.2 Results and Discussion

Numerical Phantom

The three single orientation QSM algorithms were used to calculate the susceptibility from the numerical phantom. The strength of the thresholding and filtering was varied in order to observe their effect on the calculated susceptibility. The strength of the smoothing term in the spatial domain regularization was similarly varied. The results at five different strengths are shown in Figure 4.5 below.

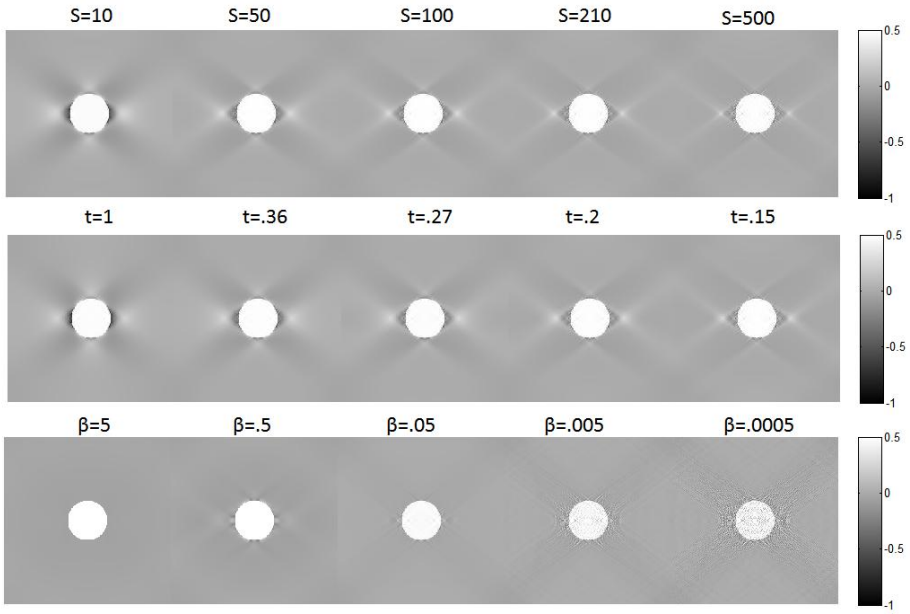

Figure 4.5: A sagittal view through the middle of the susceptibility calculated from the numerical phantom using each algorithm. The top row is the filtered transfer function, the middle row is thresholding, and the bottom row is spatial domain regularization

In Figure 4.5 above, the images are organized such that the strength of the relevant parameter increases from right to left. The strength of the threshold and the filter were calibrated to yield similar degrees of underestimation for the calculated susceptibility. As seen in Figure 4.5, the transfer function filtering operation specified by equation 4.10 and the thresholding algorithm of equation 4.5 yielded very similar results for the equivalent parameter strengths. For both cases, the streaking artifacts become more localized at the cost of greater error close to the edges as the strength of the parameter increases. The smoothing constraint of the spatial domain regularization method was much more effective at removing streaking artifacts as shown in the phantom. As seen in the bottom left image of Figure 4.5, the spatial domain regularization method provides a good estimate of the original susceptibility with little to no artifacts.

The mean squared error of each quantitative susceptibility map as well as the average calculated susceptibility within the sphere was measured while varying the strength of the regularization. For the frequency domain techniques, the optimal balance between regularization strength and accuracy was found by balancing the mean squared error over the entire image and the calculated susceptibility within the sphere.

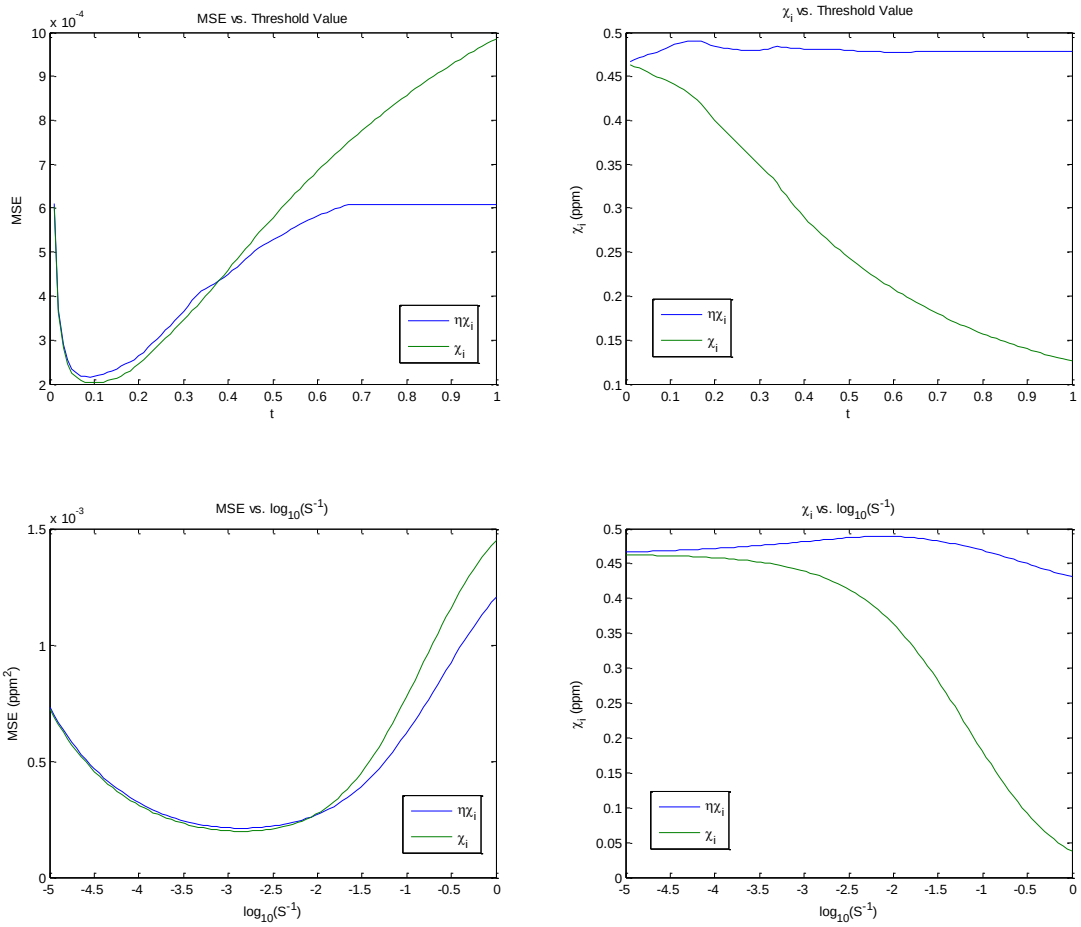

Figure 4.6: The MSE and calculated susceptibility within the sphere as the regularization strength is increased for thresholded inversion (top) and filtered inversion (bottom)

The optimal threshold was found to be t= .16, while the optimal filter strength was found to be S=117 based on Figure 4.6 above. Figure 4.6 also verifies the use of the energy loss compensation constant, η, in equations 4.5 and 4.10. As seen in Figure 4.6, the energy loss compensation greatly increases the accuracy of the calculated susceptibility in the sphere while significantly decreasing mean squared error throughout the image at higher regularization strengths.

Mean squared error and the calculated susceptibility inside each sphere was also calculated as a function of the spatial domain regularization parameter β as shown in Figure 4.7 below.

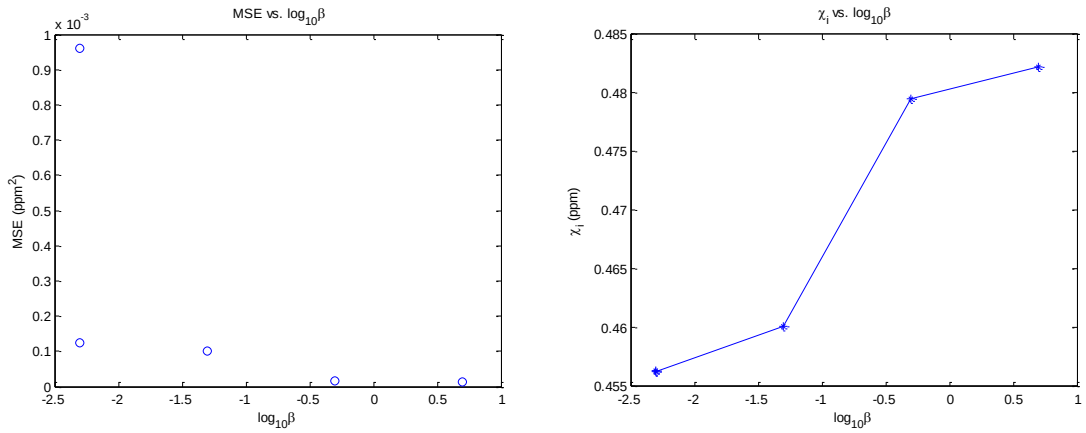

Figure 4.7: MSE and calculated susceptibility as a function of the spatial domain regularization parameter β

The optimal mean square error and the calculated susceptibility within the sphere is summarized for the three algorithms in Table 4.2 below.

Table 4.2: A comparison of the optimum MSE and calculated susceptibility between thresholded inversion, filtered inversion, and spatial domain regularization

	Threshold	Filtered	Spatial Domain Regularization
Strength	t=.16	S=117	β=5
MSE	2.403e-4 ppm^2	2.600e-4 ppm^2	1.38e-5 ppm^2
χ_i	.4904 ppm	.4891 ppm	.4822 ppm

As seen in Table 4.2 above, the spatial domain regularization had the lowest mean squared error while both frequency domain algorithms performed similarly in terms of calculated susceptibility and overall mean squared error. The improvement in mean squared error of the spatial domain regularization technique can be easily seen as a reduction in streaking artifacts in Figure 4.5 above.

MR Phantom

Quantitative susceptibility maps were generated from the phase of the GRE images of phantoms with susceptibilities calculated by gadolinium concentration. The $T2^*$ of the spheres within the phantom was measured, because dilution during the phantom filling process was suspected. The gadolinium concentration should decrease linearly with the log of the $T2^*$.

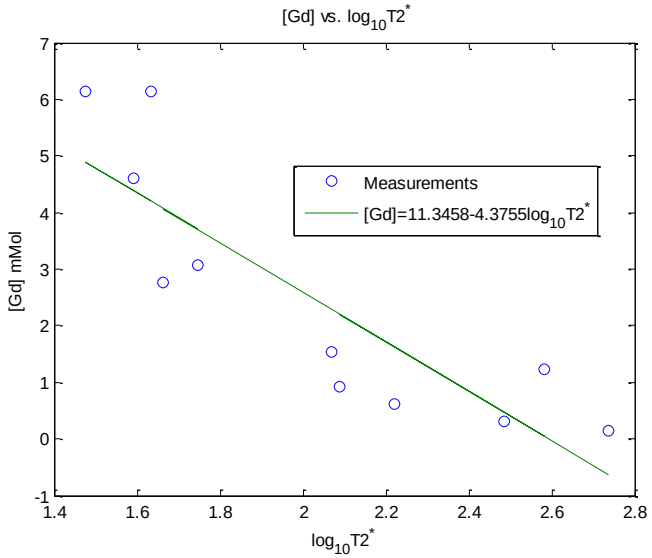

Figure 4.8: The relationship between the gadolinium concentration and the log of $T2^*$ is expected to be linear

As seen in Figure 4.8, two spheres were suspected of having incorrect gadolinium concentrations and were not incorporated in the susceptibility measurements.

The susceptibility in each sphere was measured and tabulated in Table 4.3 below.

Table 4.3: Susceptibility measured in each sphere for QSM's generated using three different algorithms

	Susceptibility (ppm)	Measured		
		Filter S=117	Threshold t=0.16	Spatial Domain α=15, β=5
Phantom 1	.20	.2349	.2824	.1711
	.47	.6097	.5548	.4250
	.88	.8331	.7637	.645
	2.06	bad	bad	bad
Phantom 2	.5	.204	.1762	.0877
	1.04	.76	.5996	.4968
	1.47	1.301	.9431	.8814
	2.00	1.2354	1.0856	.9445
Phantom 3	.05	.0644	.0602	.045
	.10	.1677	.1431	.101
	.30	.3027	.2406	.24
	.40	bad	bad	bad

The measured susceptibilities were graphed against the actual susceptibilities based on the gadolinium concentration in the spheres.

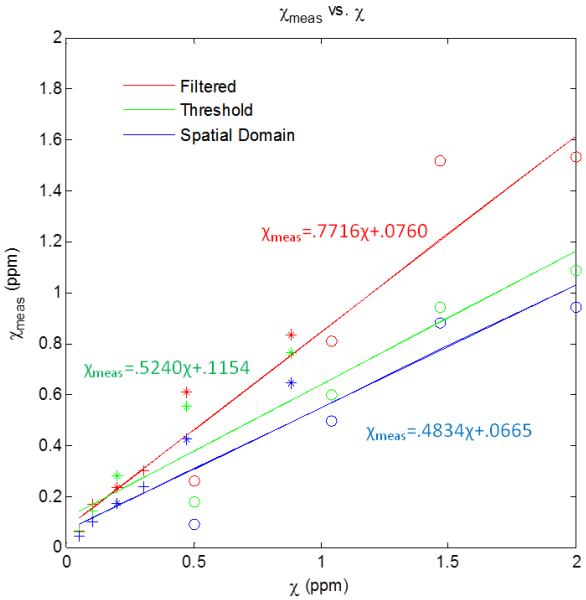

Figure 4.9: The measured susceptibility compared to the actual susceptibility. The symbols denote data points taken from the three different phantoms

As seen in Figure 4.9, above the filtered inversion algorithm produced the most accurate results. The thresholded inversion and the spatial domain regularization methods both underestimated the susceptibility to a greater extent than the filtered inversion algorithm. This result contradicts current literature which states that frequency domain methods underestimate susceptibility compared to spatial domain methods. Several factors may explain this discrepancy. The correction factor applied to the frequency domain methods greatly alleviates the underestimation problem with frequency domain methods as demonstrated on the numerical phantom. Also, the measured susceptibility seems to be fairly consistent between algorithms, which suggests that the concentration of the gadolinium may not have been accurate. This is further supported by the $T2^*$ measurements in Figure 4.8. The higher concentrations of gadolinium tended to have lower T2* constants than expected. Since the phantom was constructed with the lowest concentrations first, the higher concentration solutions may have been diluted by residual solution in the balloon.

Although the filtered inversion performed the best numerically, the spatial domain regularization method did a much better job of artifact reduction compared to both the thresholded inversion and filtered inversion as seen in Figure 4.10 below.

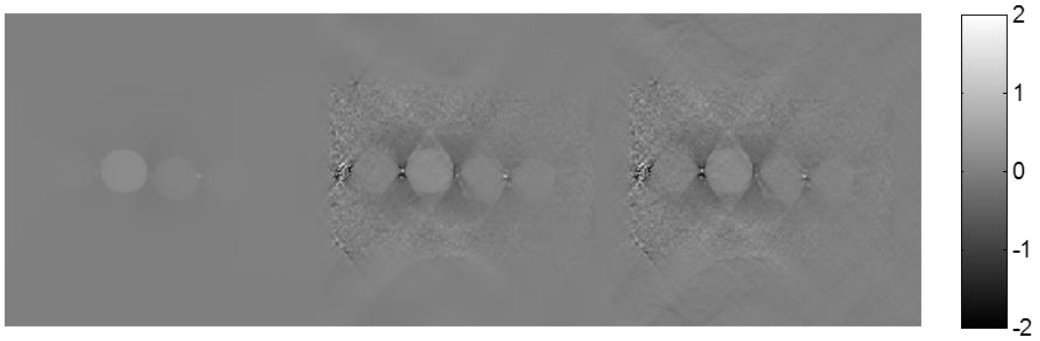

Figure 4.10: Coronal view of phantom 3. From left to right: the result from the spatial domain regularization, the filtered inversion, and the thresholded inversion

In vivo example

Susceptibility maps were calculated of the brain of a MS patient using the optimal regularization strengths for the frequency domain methods found using the numerical phantom. The regularization parameters were α=15, β=.05 for the spatial domain regularization algorithm. A lower β was necessary to prevent over-smoothing of the fine details in the brain. A comparison of the results from each single orientation method has been included in Figure 4.11 below.

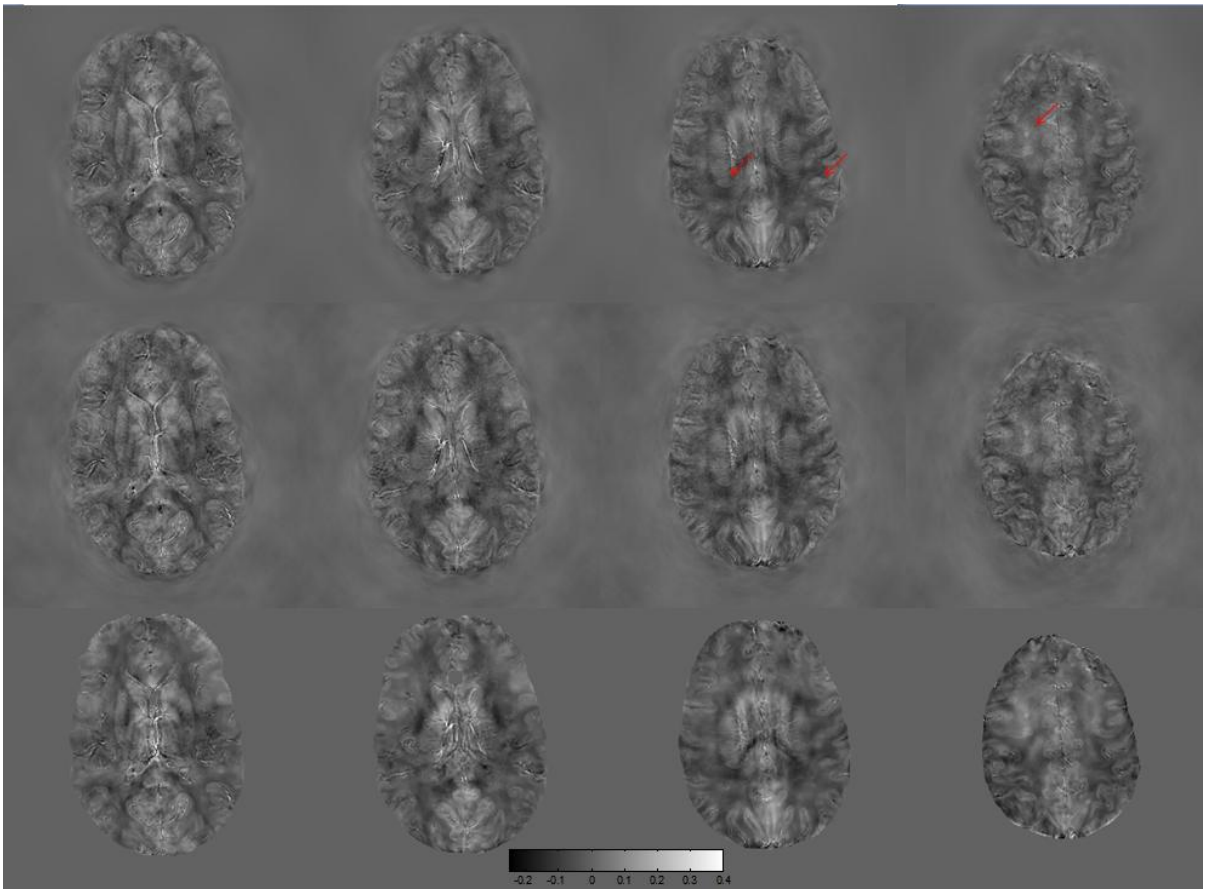

Figure 4.11: Various slices from quantitative susceptibility maps generated from the brain of an MS patient using transfer function filtering (top row), transfer function thresholding (middle row), and spatial domain regularization (bottom row)

As seen in Figure 4.11 above, the susceptibility map generated by the filtered inversion method reduces artifacts slightly better than the thresholded inversion method as evidenced by less streaking artifacts extending from the brain. Both methods provided similar differentiation

between white matter and grey matter and between lesions and the surround tissue. Although the regularized inversion method did an improved job of reducing streaking artifacts, there is noticeable blurring of the image due to the gradient regularization terms attempts to enforce a piece-wise constant solution.

The regions around the lesions denoted by the red arrows on Figure 4.11 are examined in Figure 4.12 below.

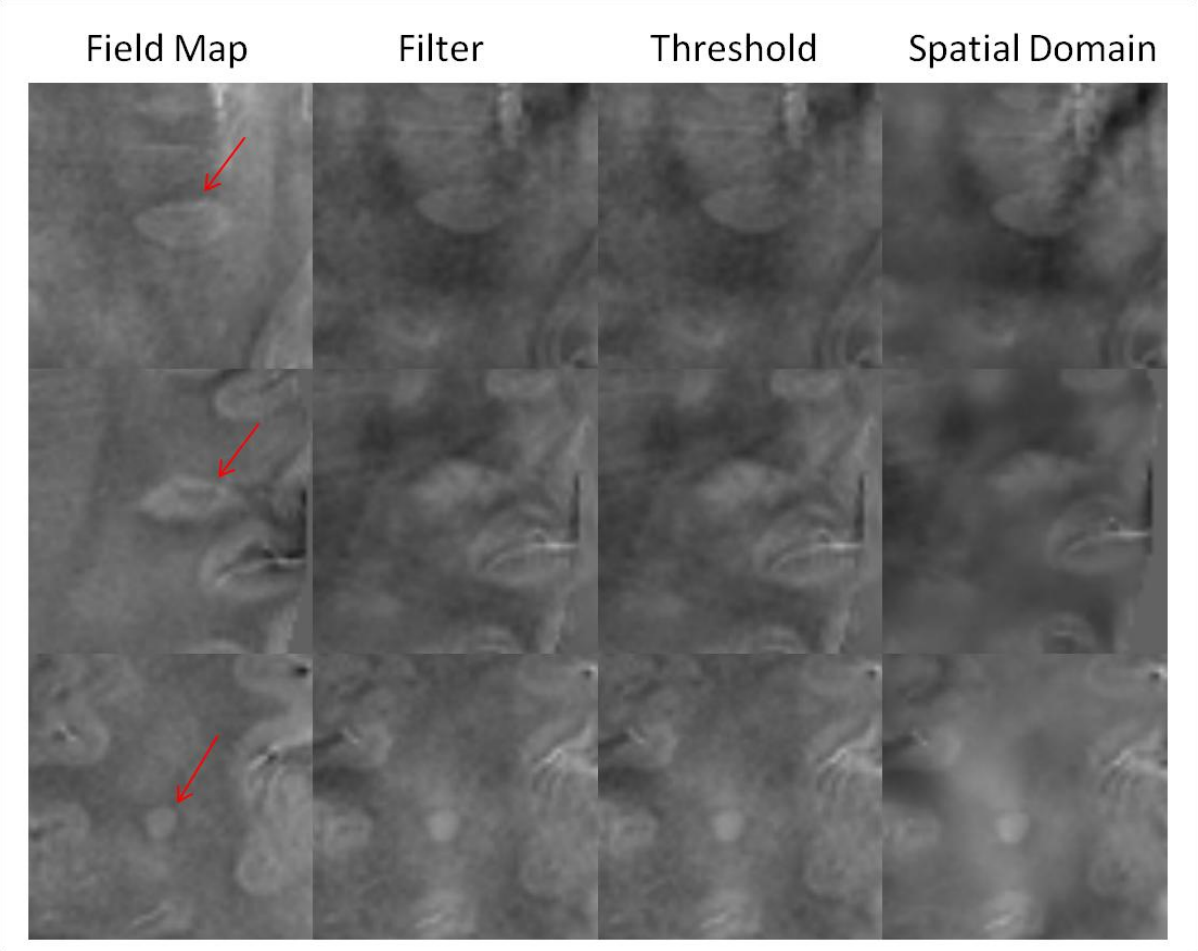

Figure 4.12: The appearance of lesions on the field map and each of the QSM methods

As seen in 4.12, the depiction of the lesions is similar in each of the QSM methods with the exception of the smoothing caused by the spatial domain regularization. The hyperintense rings

evident around the periphery of the top two lesions is absent in all the QSM's. This result suggests that the difference in appearance of lesions on QSM compared to phase images is significant for the study of multiple sclerosis.

4.4 Conclusions

Regularization techniques either in the frequency domain or in the spatial domain are necessary to generate quantitative susceptibility maps from the magnetic field shifts measured using GRE MRI sequences. Although accurate, artifact free quantitative susceptibility maps can be generated by acquiring multiple images at different orientations with respect to the main magnetic field, this method has limited utility, because it requires several long scans and requires the patient to hold their head in awkward positions. Different head positions also may not be possible due to the design of the RF coils.

Several single orientation methods were tested including a novel *k*-space filter method. The frequency domain methods performed very similarly on both phantom and in vivo data. The spatial domain regularization method was found to perform significantly better in terms of artifact reduction on phantom data. However on in vivo data, the complexity of the images makes choosing gradient penalty masks difficult. Also, it was difficult to balance image smoothing with artifact reduction on in vivo images by adjusting the strength of the regularizing parameters. For the added effort taken to calibrate the images, the final in vivo susceptibility calculations from spatial domain regularization did not differ significantly in terms of tissue contrast and lesion depiction.

The depiction of lesions in the QSM differed significantly from their depiction in phase images. Often in phase images, there is a hyperintense ring around the periphery of MS lesions. In two

cases examined in the in vivo example, the hyperintense rings were eliminated by the QSM processing. Since the presence of these hyperintense rings have been thought to indicate active demyelination at the edge of MS lesions, their absence in QSM may have clinical significance, and warrants further investigation.

CHAPTER 5

Conclusion and Future Work

5.1 Summary

Multiple sclerosis (MS) is an autoimmune disease in which myelin in the central nervous system is destroyed. The progression of the disease is tracked by characterizing the lesions caused by the demyelination and subsequent destruction of nerve cells. The pattern of iron deposition within MS lesions has been thought to indicate specific processes in MS pathology. A method of visualizing and quantifying iron in MS lesions would provide additional insight into the inflammatory process in multiple sclerosis, and assist in assessing the effectiveness of current medications. Developments in high field magnetic resonance (MR) phase imaging have shown promise as a method of generating quantitative susceptibility maps, which can be correlated to iron concentration in the brain.

The phase of gradient recalled echo (GRE) magnetic resonance images is sensitive to changes in magnetic field caused by variations in the magnetic susceptibility of tissue and thus can be used as a measure of tissue susceptibility. Calculating tissue susceptibility from GRE phase images has two primary challenges. First, the acquired phase images from the scanner are a superposition of magnetic field distortions from tissue susceptibility as well as main magnetic field inhomogeneities, RF phase, and distortions from susceptibility changes outside the field of

view. These effects must be removed in order to extract the field distortions due to tissue susceptibility. Only after the removal of extraneous field effects can the phase image be used to generate quantitative susceptibility maps.

Three established methods and one novel method for calculating and removing extraneous field effects were described in this thesis. Polynomial fitting and homodyne high pass filtering approximates the extraneous field effects as a slowly varying quantity and aims to remove the extraneous effect by fitting with a polynomial function and a complex exponential respectively. Although relatively easy to implement, both methods were shown to have severe limitations. Polynomial fits are limited to 5^{th} order polynomials due to the computational complexity of higher order fits. This was found to be insufficient for accurate modeling of the extraneous magnetic field. While high pass filtering can be done quickly and without the need of unwrapping the phase, homodyne high pass filtering inevitably removes tissue contrasts in large-scale structures in the brain such as the basal ganglia. Projection onto dipole fields (PDF) showed much more promise as a means of distinguishing between tissue field effects and extraneous effects. Although PDF had difficulty removing extraneous fields at the edges of the brain and near tissue air interfaces, PDF was found to do the best job of retaining tissue contrast, while removing the extraneous field in an in vivo comparison between polynomial fitting, homodyne filtering and PDF. A novel method, short TE scaling, based on acquiring additional data rather than modeling the field effects was developed and tested. Although the performance of the new method showed promise, additional development is needed to account for effects such as *k*-space offsets between echoes.

The second challenge of calculating magnetic susceptibility maps using phase images is the inversion of the forward model from susceptibility distribution to its effect on the magnetic field.

The inversion problem is ill-posed due to zeroes in the *k*-space transfer function which describes the frequency domain between the susceptibility distribution and the magnetic field shift. Unless a regularization technique is employed, the solution to the ill-posed problem will show significant artifacts and degradations in the image quality.

Frequency domain thresholding, spatial domain regularization, and a novel technique based on the Wiener deconvolution were described and compared in this thesis. The most significant improvement found using the frequency domain filtering technique was a lack of smoothing and faster computation time compared to spatial domain regularization, and less underestimation of the susceptibility without increased artifacts compared to frequency domain thresholding. The improvement was primarily due to using a filter with a smooth transition between the pass-band and stop-band to eliminate artifacts caused by a sharp transition and the use of a correction factor to replace energy lost in the filtering operation. The new method was calibrated and verified using numerical phantoms and MR test objects.

Finally, the algorithms developed for this thesis were used to generate QSM of a multiple sclerosis patient. The depiction of lesions in QSM was found to differ significantly from their appearance on phase images. Previously, neurologists had noted hyperintensities in the field map (scaled phase map), which were thought to indicate the presence of iron-rich macrophages actively demyelinating the periphery of MS lesions. Some of the hyperintense rings were found to be significantly attenuated or missing altogether on the QSM maps. This finding suggests that QSM provides a different and potentially more accurate representation of inflammation in MS.

5.2 Future Work

Further work should be done to validate the novel filtered frequency domain QSM method presented in this thesis. The experimental phantom results showed a significant underestimation compared to the numerical phantom data. Possible sources of these deviations include imperfect separation of the extraneous field from tissue susceptibility effects, low SNR in the phantom images, and potential error in the concentration of the gadolinium solutions during the construction of the phantoms. SNR could be improved by using longer TR, and using a base concentration of gadolinium to improve signal outside the spheres. Also, the spheres should be limited more to the center of the cylinder to avoid field effects at the periphery of the phantom, which can result in error in the generation of the field map. Finally, a more precise measurement of the expected susceptibility shift in the phantom could be found by calibrating the concentration of the gadolinium to $T2^*$. Optimizing the construction and acquisition of the MR test objects would assist in the calibration and validation of the filtered inversion algorithm. This would determine if the optimal value of the filter strength is consistent between numerical and experimental images.

Preliminary use of the QSM algorithm on *in vivo* MS images indicated that the depiction of lesions in QSM differed in a clinically significant manner from those in phase images. A comparison of the appearance of MS lesions in a statistically significant number of patients should be conducted to verify these preliminary findings. The appearance of lesions on QSM should also be correlated with findings in histology. Verifying the difference in appearance of MS lesions between phase and QSM would validate that QSM provides a different and more accurate picture of inflammatory activity compared to phase imaging alone.

Finally, the QSM algorithm developed in this thesis should be applied to longitudinal studies of MS patients. QSM provides a potentially more detailed and accurate assessment of inflammatory activity in the brain, and would be a useful measure of the efficacy of drug treatments on MS patients.

REFERENCES

[1] V. Mehta et al. “Iron is a Sensitive Biomarker for Inflammation in Multiple Sclerosis Lesions," *PLOS ONE*, vol. 8 pp. 1-10, Mar.. 2013.

[2] David Pitt et al. “Imaging Cortical Lesions in Multiple Sclerosis with Ultra-High-Field Magnetic Resonance Imaging.” *Archives Neurology,* vol. 67(7), pp. 812-818, 2010.

[3] J. F. Schenck, “The role of magnetic susceptibility in magnetic resonance imaging: MRI magnetic compatibility of the first and second kinds,” *Med. Phys.*, vol. 23 pp. 815-849, Feb. 1996.

[4] J. P. Marques, R. Bowtell, “Application of a Fourier-based method for rapid calculation of field inhomogeneity due to spatial variation of the magnetic susceptibility,” *Concepts in Mag. Res. Part B: Mag. Res. Eng,* vol. 25B(1), pp. 65-78, Oct. 2004.

[5] Salomir et al. “A Fast Calculation Method for Magnetic Field Inhomogeneity due to an Arbitrary Distribution of Bulk Susceptibility.” *ERT Imagerie moleculaire et fonctionnelle*, vol. 117, pp. 26-34, July 2003.

[6] M. Jenkinson, “Fast, Automated, N-Dimensional Phase Unwrapping Algorithm,” *Magn. Res. in Med.*, vol. 49, pp. 193-197, Aug. 2002.

[7] R. Shewchuck, *An Introduction to the Conjugate Gradient Method Without the Agonizing Pain*, PA, Carnegie Mellon University, 1994.

[8] A.M. Abduljalil, “Enhanced gray and white matter contrast of phase susceptibility-weighted images in ultra-high-field magnetic resonance imaging,” *J. Magn. Res. Imaging*, vol. 18, pp. 284-290, Sept. 2003.

[9] Tian Liu et al. “A novel background field removal method for MRI using projection onto dipole fields (PDF),” *NMR in Biomed.*, vol. 24, pp 1129-1136, Dec. 2010.

[10] Tian Liu et al. “Calculation of Susceptibility Through Multiple Orientation Sampling (COSMOS): A Method for Conditioning the Inverse Poblem From Measured Magnetic Field Map to Susceptibility Source Image in MRI,” *Magn. Res. in Med.*, vol. 61, pp. 196-204.

[11] Ludovic de Rochefort et al. “Quantitative Susceptibility Map Reconstruction from MR Phase Data Using Bayesian Regularization: Validation and Application to Brain Imaging,” *Magn. Res. in Med.*, vol. 63, pp. 194-206, Jul. 2009.

[12] Wharton et al. “Susceptibility Mapping in the Human Brain Using Threshold-Based *K*-Space Division.” *Magnetic Resonance in Medicine*, vol. 63, pp. 1292-1304, Nov. 2010.

[13] Karin Shmueli et al. “Magnetic Susceptibility Mapping of Brain Tissue In Vivo Using MRI Phase Data,” *Magn. Res. in Med.*, vol. 62, pp. 1510-1522, Oct. 2009.

[14] Rice University. “Wiener Filtering,” Internet: http://www.owlnet.rice.edu/~elec539/Projects99/BACH/proj2/blind/bd.html, [Oct. 9, 2011].

APPENDIX A: MATLAB CODE

Salomir Transfer Function

```
function [ H ] = salomirtf( dimension,dx,dy,dz,orientation )
%creates the salomir transfer function in k-space given a volume size and
%resolution.  Volume size is the number of voxels in a direction, while the
%resolution is the dimension of the voxels in mm. scanner coordinate system
%used
%Dimension is the dimensions of the (desired image) in terms of [rows,
%columns, slices, echos]
%%orientation refers to patient orientation with respect to the magnetic field orientation.
%it is a string that specifies the orientation of the patient's body
%with respect to the magnetic field.  Default is axial, choices are axial,
%sagittal and coronal

   %check for odd dimensions;

if mod(dimension(3),2)==1
   dimension(3)=dimension(3)-1;
end
%y direction
if mod(dimension(1),2)==1
   dimension(1)=dimension(1)-1;
end
%x direction
if mod(dimension(2),2)==1
   dimension(2)=dimension(2)-1;
end

if strcmp(orientation,'sagittal')==1
   Nz=dimension(1);
   Ny=dimension(2);
   Nx=dimension(3);
   %calculate sample width in k space
   dKx=2*pi/Nx/dx;
   dKy=2*pi/Ny/dy;
   dKz=2*pi/Nz/dz;
   %--------------------------------------------------------------------------
   %construct Salomir Filter Transfer Function
   Kx=[0:1:(floor(Nx/2)-1) -(floor(Nx/2)):1:-1]*dKx;
   temp=ones(dimension(1:3));
   for n=1:Nx
      temp(:,:,n)=Kx(n);
   end
   Kx=temp;
   Ky=[0:1:(floor(Ny/2)-1) -(floor(Ny/2)):1:-1]*dKy;
   Ky=Ky';
   for n=1:Ny
      temp(n,:,:)=Ky(n);
   end
   Ky=temp;
   Kz=[0:1:(floor(Nz/2)-1) -(floor(Nz/2)):1:-1]*dKz;
   for n=1:Nz
      temp(:,n,:)=Kz(n);
   end
   Kz=temp;
```

```
    H=ones(dimension);
    A=Kz.^2;
    B=(Kx.^2+Ky.^2+Kz.^2);
    B(find(B==0))=1*10^-10;
    H=1/3-A./B;

elseif strcmp(orientation,'coronal')==1
    Nz=dimension(1);
    Nx=dimension(2);
    Ny=dimension(3);
    %calculate sample width in k space
    dKx=2*pi/Nx/dx;
    dKy=2*pi/Ny/dy;
    dKz=2*pi/Nz/dz;

    %--------------------------------------------------------------------------
    %construct Salomir Filter Transfer Function
    Kx=[0:1:(floor(Nx/2)-1) -(floor(Nx/2)):1:-1]*dKx;
    temp=ones(dimension(1:3));
    for n=1:dimension(2)
       temp(:,n,:)=Kx(n);
    end
    Kx=temp;
    Ky=[0:1:(floor(Ny/2)-1) -(floor(Ny/2)):1:-1]*dKy;
    Ky=Ky';
    for n=1:dimension(3);
       temp(:,:,n)=Ky(n);
    end
    Ky=temp;
    Kz=[0:1:(floor(Nz/2)-1) -(floor(Nz/2)):1:-1]*dKz;
    for n=1:dimension(1)
       temp(n,:,:)=Kz(n);
    end
    Kz=temp;
    H=ones(dimension);
    A=Kz.^2;
    B=(Kx.^2+Ky.^2+Kz.^2);
    B(find(B==0))=1*10^-10;
    H=1/3-A./B;
else
    Ny=dimension(1);
    Nx=dimension(2);
    Nz=dimension(3);
    %calculate sample width in k space
    dKx=2*pi/Nx/dx;
    dKy=2*pi/Ny/dy;
    dKz=2*pi/Nz/dz;
    %--------------------------------------------------------------------------
    %construct Salomir Filter Transfer Function
    Kx=[0:1:(floor(Nx/2)-1) -(floor(Nx/2)):1:-1]*dKx;
    temp=ones(dimension(1:3));
    for n=1:dimension(2)
       temp(:,n,:)=Kx(n);
    end
    Kx=temp;
    Ky=[0:1:(floor(Ny/2)-1) -(floor(Ny/2)):1:-1]*dKy;
```

```
    Ky=Ky';
    for n=1:dimension(1);
        temp(n,:,:)=Ky(n);
    end
    Ky=temp;
    Kz=[0:1:(floor(Nz/2)-1) -(floor(Nz/2)):1:-1]*dKz;
    for n=1:dimension(3)
        temp(:,:,n)=Kz(n);
    end
    Kz=temp;
    H=ones(dimension);
    A=Kz.^2;
    B=(Kx.^2+Ky.^2+Kz.^2);
    B(find(B==0))=1*10^-10;
    H=1/3-A./B;
end
end
```

Gradient Matching Unwrapping Algorithm

```
% 3D phase unwrapping
clear
clc

%Load wrapped phase image
file=open_nifti;
dimension=size(file.img);
modphase=file.img;

%Load image mask
file1=open_nifti;
file1=file1.img(:,:,:);%,dimension(4));
mask=zeros(size(file1));
mask(file1~=0)=1;
clear file1
%se = strel('disk',6,6);
%erodedmask = imerode(mask(:,:,slice),se);

%Apply mask to wrapped phase image
for echo=1:dimension(4)
   modphase(:,:,:,echo)=modphase(:,:,:,echo).*mask;
end

% %Find base phase based on linearity
%     TE0=1;
%     dTE=1;
%     X=[TE0:dTE:TE0+dTE*(dimension(4)-1)]';%how uniform is TE across the image?
%     X=[ones(size(X)),X];
%
% rsq=zeros(dimension(1:3));
% tic
% for x=1:dimension(1)
%     for y=1:dimension(2)
%         for z=110:140
%             if mask(x,y,z)~=0
%                 Y=squeeze(modphase(x,y,z,:));
%                 [b,~,r]=regress(Y,X);
%                 rsq(x,y,z)=1-sum(r.^2)./(sum(Y.^2));
%             end
%         end
%     end
% end
toc

%% Uncomment if computer has >16 GB of RAM
% %Find gradient of unwrapped image
% tic
% %Calculate the gradient of the image for a variety of phase offsets
% for echo=1:dimension(4)
%     for theta=1:5
%
[phasegradx{echo}(:,:,:,theta),phasegrady{echo}(:,:,:,theta),phasegradz{echo}(:,:,:,theta)]=cdiff3(angle(exp(1i*(mo
dphase(:,:,:,echo)+theta*pi/5))),1,1,1,'r');
```

```
%     phasegradx{echo}(:,end,:,theta)=0;%last row is not accurate due to convolution
%     phasegrady{echo}(end,:,:,theta)=0;%last row is not accurate due to convolution
%     phasegradz{echo}(:,:,end,theta)=0;%last slice is not accurate due to convolution
%     end
% end
%
% %Filter out the unreliable gradient data where the image is wrapped
% for echo=1:dimension(4)
%     mphasegradx{echo}=median(phasegradx{echo},4);
%     mphasegrady{echo}=median(phasegrady{echo},4);
%     mphasegradz{echo}=median(phasegradz{echo},4);
% end
% toc
% clear phasegradx phasegrady phasegradz

%% Find gradient of unwrapped image--Use if computer has <16 GB of RAM
tic
for echo=1:dimension(4)
   for theta=1:5
      phasegradx{echo}(:,:,:,theta)=convn(angle(exp(1i*(modphase(:,:,:,echo)+theta*pi/5))),[1,-1],'same');
      phasegradx{echo}(:,end,:,theta)=0;%last row is not accurate due to convolution
   end
   mphasegradx{echo}=median(phasegradx{echo},4);
end

clear phasegradx

for echo=1:dimension(4)
   for theta=1:5
      phasegrady{echo}(:,:,:,theta)=convn(angle(exp(1i*(modphase(:,:,:,echo)+theta*pi/5))),[1,-1]','same');
      phasegrady{echo}(end,:,:,theta)=0;%last column is not accurate due to convolution
   end
   mphasegrady{echo}=median(phasegrady{echo},4);
end

clear phasegrady

for echo=1:dimension(4)
   for theta=1:5
      z=ones(1,1,2);
      z(:,:,2)=-1;
      phasegradz{echo}(:,:,:,theta)=convn(angle(exp(1i*(modphase(:,:,:,echo)+theta*pi/5))),z,'same');
      phasegradz{echo}(:,:,end,theta)=0;%last slice is not accurate due to convolution
   end
   mphasegradz{echo}=median(phasegradz{echo},4);
end

clear phasegradz
toc

%% Perform conjugate gradients minimization to find unwrapped phase based on
%gradients and offset
tic
Unwrapped=zeros(dimension);
for echo=1:dimension(4)
```

```
Unwrapped(:,:,:,echo)=GradientMatch(Unwrapped(:,:,:,echo),mphasegradx{echo},mphasegrady{echo},mphasegrad
z{echo},500);
end
toc


function [ U ] = GradientMatch( U,dPhix,dPhiy,dPhiz,n )
%Function Description:
%This function uses conjugate gradients to find the solution to:
% minU ||GxU-dPhix||^2+||GyU-dPhiy||^2+||GzU-dPhiz||^2+||MU-MPhi||^2
%where Gx is the gradient matrix
%M is a diagonal matrices representing 3D image masks representing areas of
%reliable phase (as determined by linear propagation with TE
%U is the solution
%dPhix is the observed gradient in x
%dPhiy is the observed gradient in y
%dPhiz is the observed gradient in z
%Phi is the wrapped phase data
%n is the maximum number of iterations
%% Intended Purpose
%although useable for any problem with the above form, this function was
%written expressly for the purpose of performing phase unwrapping.  The
%iterative method should avoid problems due to error propagation by a
%straight integration
%% Initialize vectors and parameters
i=0; %counts number of iterations
epsq=1E-8;%tolerance

%Compute residual (r=b-Ax)
   %compute Ax
      %compute Gx'GxU
      GxGxU=convn(convn(U,[1,-1],'valid'),[-1,1],'full');
      %compute Gy'GyU
      GyGyU=convn(convn(U,[1,-1]','valid'),[-1,1]','full');
      %compute Gz'GzU
      z=ones(1,1,2);
      z(:,:,2)=-1;
      GzGzU=convn(convn(U,z,'valid'),-z,'full');
   Ax=GxGxU+GyGyU+GzGzU;
   %compute b
      %compute Gx'dPhix
      GxdPhix=convn(dPhix(:,1:end-1,:),[-1,1],'full');
      %compute Gy'dPhiy
      GydPhiy=convn(dPhiy(1:end-1,:,:),[-1,1]','full');
      %compute Gy'dPhiz
      GzdPhiz=convn(dPhiz(:,:,1:end-1),-z,'full');
   b=GxdPhix+GydPhiy+GzdPhiz;
r=b-Ax;

%initialize first and next search direction
d=r;
%reshape residual as a column vector
dnew=sum(sum(sum(r.^2)));%r'*r;
d0=dnew;
```

```
%iterate
while i<n && dnew>epsq*d0
   %calculate q=Ad using convolutions
      %compute Gx'Gxd
      GxGxU=convn(convn(d,[1,-1],'valid'),[-1,1],'full');
      %compute Gy'Gyd
      GyGyU=convn(convn(d,[1,-1]','valid'),[-1,1]','full');
      %compute Gz'Gzd
      z=ones(1,1,2);
      z(:,:,2)=-1;
      GzGzU=convn(convn(d,z,'valid'),-z,'full');
   q=GxGxU+GyGyU+GzGzU;
   alpha=dnew/sum(sum(sum(d.*q)));%(d'*q);%calculate how far to make next guess
   U=U+alpha*d;
   if ceil(i/50)==i/50 && i~=0 %if divisible by 50 reinitialize residual vector
      %Compute residual (r=b-Ax)
         %compute Ax
            %compute Gx'GxU
            GxGxU=convn(convn(U,[1,-1],'valid'),[-1,1],'full');
            %compute Gy'GyU
            GyGyU=convn(convn(U,[1,-1]','valid'),[-1,1]','full');
            %compute Gz'GzU
            z=ones(1,1,2);
            z(:,:,2)=-1;
            GzGzU=convn(convn(U,z,'valid'),-z,'full');
         Ax=GxGxU+GyGyU+GzGzU;
         %compute b
            %compute Gx'dPhix
            GxdPhix=convn(dPhix(:,1:end-1,:),[-1,1],'full');
            %compute Gy'dPhiy
            GydPhiy=convn(dPhiy(1:end-1,:,:),[-1,1]','full');
            %compute Gy'dPhiz
            GzdPhiz=convn(dPhiz(:,:,1:end-1),-z,'full');
         b=GxdPhix+GydPhiy+GzdPhiz;
      r=b-Ax;
      Figure ()
      imshow(U(:,:,125),[])
      title(['After' num2str(i) 'Iterations'])

   else
      r=r-alpha*q;
   end
      dold=dnew;
      dnew=sum(sum(sum(r.^2)));%r'*r;
      beta=dnew/dold;
      d=r+beta*d;
      %hold on
      %plot(i,dnew,'o')
      i=i+1
end
end
```

Homodyne High Pass Filter

```
function [ phaseims ] = homodyne( ims, strength )
%This function takes a complex image input, and outputs the homodyne high
%pass filtered phase image
%   Strength gives the strength of the HPF

dimension=size(ims);

%check for data sets with only one echo
if size(dimension)<4
   dimension=[dimension,1];
end

%set filter strength (the 3dB cutoff point (pixels measured from the center) as a percent of Kx or Ky)
x1=dimension(1)/2*strength;
sig=sqrt(-.5*x1^2/log10(1/sqrt(2)));
sigky=sig;
sigkx=sig;

%create filter
h=[dimension(1),dimension(2)];

for x=1:dimension(1)
   parfor y=1:dimension(2)
      h(x,y)=exp(-.5*((x-dimension(1)/2)^2/sigkx^2+(y-dimension(2)/2)^2/sigky^2));
   end
end

phaseims=ones(dimension);
k=0;

for echo=1:dimension(4)
   parfor z=1:dimension(3)
      tmp(:,:,z,echo)=fft2(ims(:,:,z,echo));
      tmp(:,:,z,echo)=fftshift(tmp(:,:,z,echo));
      tmp(:,:,z,echo)=tmp(:,:,z,echo).*h;
      tmp(:,:,z,echo)=fftshift(tmp(:,:,z,echo));
      LPFim(:,:,z,echo)=ifft2(tmp(:,:,z,echo));
      phaseims(:,:,z,echo)=ims(:,:,z,echo)./LPFim(:,:,z,echo);
      phaseims(:,:,z,echo)=angle(phaseims(:,:,z,echo));
   end
   k=k+1;
   fprintf(['Finished Echo ' num2str(k) '\n'])
end

clear tmp
clear LPFim

fprintf('finished filtering \n')


end
```

Polynomial Fitting

```
function [ fit ] = polyfitn( image, mask, n )
%POLYFITN This function computes the best fit nth order polynomial of an image by
%least squares minimization over an area defined by mask

dimension=size(image);
[X,Y,Z]=meshgrid(-dimension(1)/2:dimension(1)/2-1,-dimension(2)/2:dimension(2)/2-1,-
dimension(3)/2:dimension(3)/2-1);
%columnize everything
X=reshape(mask.*X,dimension(1)*dimension(2)*dimension(3),1);
Y=reshape(mask.*Y,dimension(1)*dimension(2)*dimension(3),1);
Z=reshape(mask.*Z,dimension(1)*dimension(2)*dimension(3),1);
counter=1;
coeff=[];
for order=1:n
      for xorder=1:order
         for yorder=0:order-xorder;
            zorder=order-xorder-yorder;
            coeff(counter,:)=[xorder,yorder,zorder];
            counter=counter+1;
         end
      end
      for yorder=1:order
         zorder=order-yorder;
         coeff(counter,:)=[0,yorder,zorder];
         counter=counter+1;
      end
      coeff(counter,:)=[0,0,order];
      counter=counter+1;
end
coeff(counter,:)=[0,0,0];

VtV=[];
for x=1:length(coeff)
   for y=1:length(coeff)
      VtV(x,y)=(X.^coeff(x,1).*Y.^coeff(x,2).*Z.^coeff(x,3))'*(X.^coeff(y,1).*Y.^coeff(y,2).*Z.^coeff(y,3));
   end
end

Vtb=[];
for x=1:length(x)
   Vtb(x,1)=(X.^coeff(x,1).*Y.^coeff(x,2).*Z.^coeff(x,3))'*b;
end

p=VtV\Vtb;

fit=0;
for x=1:length(x)
   fit=fit+p(x)*(X.^coeff(x,1).*Y.^coeff(x,2).*Z.^coeff(x,3));
end
fit=reshape(fit,dimension);
end
```

Short TE Scaling

```
%This program computes the B0 map by complex dividing and filtering a GRE
%image

%open input images

real1=open_nifti;
imaginary1=open_nifti;
ims1=real1.img(:,:,:,1)-1i*imaginary1.img(:,:,:,1);
TE1=1.48;
deltaTE1=4.8;

real2=open_nifti;
imaginary2=open_nifti;
ims2=real2.img(:,:,:,1)-1i*imaginary2.img(:,:,:,1);
TE2=1.43;
deltaTE=4.8;

%complex divide one by two to create a very short TE

ims=ims1./ims2;
nTE=TE1-TE2;

%threshold filter

%define filter size
xsize=16;
ysize=16;
zsize=16;
dimension=size(ims);
nx=floor(xsize);
ny=floor(ysize);
nz=floor(zsize);

%define mask
mask=abs(ims1);
T=.4*mean(mean(mean(mask)));
mask(mask<T)=0;
mask(mask~=0)=1;

%perform filtering operation
newims=ones(dimension);
ims=angle(ims);
matlabpool open
tic
if dimension(3)>=68;
parfor x=1:4
newims(:,:,:,x)=partandparcel(mask,ims,nx,ny,nz,x,0);
end
matlabpool close
image=zeros(dimension);
image(:,:,nz:floor((dimension(3)-nz+1)/4))=newims(:,:,nz:floor((dimension(3)-nz+1)/4),1);
```

```
image(:,:,floor((dimension(3)-nz+1)/4):floor((dimension(3)-nz+1)/2))=newims(:,:,floor((dimension(3)-
nz+1)/4):floor((dimension(3)-nz+1)/2),2);
image(:,:,floor((dimension(3)-nz+1)/2):floor((dimension(3)-nz+1)*3/4))=newims(:,:,floor((dimension(3)-
nz+1)/2):floor((dimension(3)-nz+1)*3/4),3);
image(:,:,floor((dimension(3)-nz+1)*3/4):floor(dimension(3)-nz+1))=newims(:,:,floor((dimension(3)-
nz+1)*3/4):floor(dimension(3)-nz+1),4);
else
   image=zeros(dimension);
if 1==1
for x=nx:dimension(1)-nx+1;
   for y=ny:dimension(2)-ny+1;
      for z=nz:floor(dimension(3)-nz+1);
         if mask(x,y,z)==1
            image(x,y,z)=sum(sum(sum(mask(x-nx+1:x+nx-1,y-ny+1:y+ny-1,z-nz+1:z+nz-1).*ims(x-nx+1:x+nx-1,y-
ny+1:y+ny-1,z-nz+1:z+nz-1))))/sum(sum(sum(mask(x-nx+1:x+nx-1,y-ny+1:y+ny-1,z-nz+1:z+nz-1))));
         end
      end
   end
end
else
   printf('filtering')
   parfor z=1:dimension(3)

      image(:,:,z)=wiener2(ims(:,:,z),[32,32]);
   end
   matlabpool close
end
end
toc
load handel;
player = audioplayer(y, Fs);
play(player);

[X,Y,Z]=meshgrid(1:448,1:448,1:.5:50.5);
newimage=interp3(image,X,Y,Z);
newimage(:,:,100)=zeros(448,448);
%scale=fminsearch(@(scale) scaleTE(scale, newimage, image,mask),625,options);
tmp=newimage*scale+offset;
tmp=exp(j*tmp);
%newimage=angle(newimage);
filt=tmp./swi;
filt=angle(filt);

%_____________________________________________________________
file=open_nifti;
reality=open_nifti;
imagination=open_nifti;
[X,Y,Z]=meshgrid(1:448,1:448,1:.5:50.5);
newimage=interp3(file.img,X,Y,Z);
newimage(:,:,100)=zeros(448,448);
mask=newimage;
mask(newimage==0)=0;
ims=reality.img+j*imagination.img;
image=ims(:,:,:,1)./ims(:,:,:,3);
```

```
i=1;
for scale=5:20
   k=1;
   for offset=0:.1:pi
   error(i,k)=scaleTE(-scale,offset,newimage,image,mask);
   k=k+1;
   end
   i=i+1;
end

%_____________________________________________________________________
tmp=newimage*scale+offset;
tmp=exp(j*tmp);
%newimage=angle(newimage);
filt=tmp./image;
filt=angle(filt);
figure (1)
imshow(filt(:,:,50),[])
[y1,x1]=getpts;
[y2,x2]=getpts;
slice=50;
slopex=((filt(floor(y2),floor(x2),slice))-(filt(floor(y1),floor(x1),slice)))/(x2-x1);
slopey=((filt(floor(y2),floor(x2),slice))-(filt(floor(y1),floor(x1),slice)))/(y2-y1);
[X,Y]=meshgrid(1:size(filt,2));
grad=Y.*slopey+X.*slopex+(filt(floor(y2),floor(x2),slice));
grad=repmat(grad,[1,1,size(filt,3)]);
grad=exp(j*grad.*slopex);
tmp=exp(j*tmp);
%newimage=angle(newimage);
filt=tmp./image.*grad;
filt(isnan(filt))=0;
filt=angle(filt);
figure (2)
imshow(filt(:,:,50),[]);

%_____________________________________________________________________
tmp=newimage*-scale+offset;%gradient correction v2
tmp=exp(j*tmp);
%newimage=angle(newimage);
slice=50;
filt=tmp./swi;
filt=angle(filt);
figure (1)
image=filt(:,:,slice);
imshow(image,[])
mask=createMask(imline());
[coeff]=polyfit(1:length(image(mask)),image(mask)',1);
[y1,x1]=find(mask,1,'first');
[y2,x2]=find(mask,1,'last');
ang=atan((y2-y1)/(x2-x1));
[X,Y]=meshgrid(1:size(filt,2));

gradx=coeff(1)*X+coeff(2)-coeff(1)*(x1-1);
gradx=imrotate(gradx,ang*180/pi,'crop');
gradx=repmat(gradx,[1,1,size(filt,3)]);
```

```
grady=coeff(1)*Y+coeff(2)-coeff(1)*(y1-1);
grady=imrotate(grady,ang*180/pi,'crop');
grady=repmat(grady,[1,1,size(filt,3)]);
tmp=exp(j*tmp);
%newimage=angle(newimage);
filt=tmp./swi./exp(j*gradx);
filt(isnan(filt))=0;
filt=angle(filt);
figure (2)
imshow(filt(:,:,50),[]);
```

Projection on Dipole Fields

```
%open nifti file
file=open_nifti;

%remove time invariant field inhomogeneity
%file.img=file.img(:,:,:,3)-file.img(:,:,:,1);
file.hdr.dime.dim(5)=1;

%ensure even number of slices
dimension=size(file.img);

%check for odd dimensions;
%z direction
if mod(dimension(3),2)==1
   file.img=file.img(:,:,1:(dimension(3)-1),:);
   file.hdr.dime.dim(4)=file.hdr.dime.dim(4)-1;
end
%y direction
if mod(dimension(1),2)==1
   file.img=file.img(1:(dimension(1)-1),:,:,:);
   file.hdr.dime.dim(2)=file.hdr.dime.dim(2)-1;
end
%x direction
if mod(dimension(2),2)==1
   file.img=file.img(1:(dimension(2))-1,:,:,:);
   file.hdr.dime.dim(3)=file.hdr.dime.dim(3)-1;
end
dimension=size(file.img);%update dimension
%check for data sets with only one echo
if size(dimension)<4
   dimension=[dimension,1];
end

%% Set parameters for conjugate gradients regularization
x=zeros(dimension);%inital guess
W=ones(dimension);
W(file.img==0)=0;%mask for error term
M=W;%mask for regularization term
n=200;%maximum iterations
a=1E6;%strength of regularization term
% resolution in m
dy=file.hdr.dime.pixdim(2)/1000;
dx=file.hdr.dime.pixdim(3)/1000;
dz=file.hdr.dime.pixdim(4)/1000;

H=salomirtf(dimension,dx,dy,dz,'axial');
for echo=1:dimension(4)
dB=DipoleProjection(x,W,H,file.img(:,:,:,echo),a,M,n);
corrected(:,:,:,echo)=M.*(file.img(:,:,:,echo)-dB);
end

function [ db,x ] = DipoleProjection( x,W,H,dB,a,M,n )
```

```
%Function Description:
%This function uses conjugate gradients to find the solution to:
% minx ||W(Cx-d||^2+a^2||Mx||^2
%where Cx represents a 3D convolution in matrix vector form
%W and M are diagonal matrices representing 3D image masks
%a controls the strength of the regularization term
%d is the observed solution to the convolution problem
%n is the maximum number of iterations
%% Intended Purpose
%although useable for any problem with the above form, this function was
%written expressly for the purpose of performing projection onto dipole
%filtering as a QSM preprocessing step to remove external field influences
%due to B0 or B1 inhomogeneity from unwrapped GRE phase images.

%The algorithm assumes C=C', as is the case for the unit dipole kernel!!

%% Function inputs

%Input W is a 3D mask of the brain. The mask can be based on the magnitude
%of the GRE image and used as a form of noise filtering, or it can be a
%straight mask of the brain so that only the residuals inside the brain are
%weighted. (Choose nonzero values inside the brain)

%Input H is a 3D matrix that describes the convolution kernel in the
%frequency domain

%d is a 3D matrix containing unwrapped GRE B0 maps

%a is a regularization parameter specifying the strength of the
%regularizing term

%M is a mask which is ones inside the brain and zeros outside the brain.
%This forces a solution which attempts to match the field inside the brain
%using only dipoles outside the region of interest

%n is the maximum number of iterations

%% Initialize vectors and parameters
i=0; %counts number of iterations
dimx=size(x);%find size of x
epsq=1E-8;%tolerance

%Compute residual (r=b-Ax) using FFTs
r=2*(ifftn(H.*fftn(W.^2.*dB))-ifftn(H.*fftn(W.^2.*ifftn(H.*fftn(x))))-a^2*M.^2.*x);
%initialize first and next search direction
d=r;
%reshape residual as a column vector
r=reshape(r,dimx(1)*dimx(2)*dimx(3),1);
dnew=r'*r;
d0=dnew;

%iterate
while i<n && dnew>epsq*d0
   %calculate q=Ad using FFTs
   d=reshape(d,dimx(1),dimx(2),dimx(3));%3Dize
   %d(isnan(d))=0;%prevent introduction of NaN or inf during FT
```

```
    %d(isinf(d))=0;
    q=2*(ifftn(H.*fftn(W.^2.*ifftn(H.*fftn(d))))+a^2*M.^2.*d);
    q=reshape(q, dimx(1)*dimx(2)*dimx(3),1); %columnize
    d=reshape(d, dimx(1)*dimx(2)*dimx(3),1); %columnize
    alpha=dnew/(d'*q);%calculate how far to make next guess
    x=x+alpha*reshape(d,dimx(1),dimx(2),dimx(3));
    if ceil(i/50)==i/50 && i~=0 %if divisible by 50 reinitialize residual vector
       %Compute residual (r=b-Ax) using FFTs
       r=2*(ifftn(H.*fftn(W.^2.*dB))-ifftn(H.*fftn(W.^2.*ifftn(H.*fftn(x))))-a^2*M.^2.*x);
       r=reshape(r,dimx(1)*dimx(2)*dimx(3),1);%columnize
    else
       r=r-alpha*q;
    end
       dold=dnew;
       dnew=r'*r;
       beta=dnew/dold;
       d=r+beta*d;
       i=i+1
end
db=ifftn(fftn(x).*H);
end
```

Threshold Inversion QSM Algorithm

```
function [ X ] = thresholdedinversion( image,dx,dy,dz,orientation,t )
%Calculates the susceptibility in ppm from field shifts in muT.
%dx, dy, and dz are the resolution in x, y, and z in meters
%orientation is a string specifying the orientation of the object wrt the
%main field choices are 'axial' 'sagittal' or 'coronal'
%t is the threshold of the transfer function used in the inversion

dimension=size(image);
if size(dimension<4)
   dimension(4)=1;
end
H=salomirtf(dimension(1:3),dx,dy,dz,orientation);
G=H;
G(((abs(H)<=t)&(H<=0)))=-t;
G(((abs(H)<=t)&(H>=0)))=t;
adjust=sqrt( mean(mean(mean(abs(H./G).^2))));
X=fftn(image);
%X(abs(H)<=t)=0;
for n=1:dimension(4)
X(:,:,:,n)=1/G.*X(:,:,:,n);
end
X=ifftn(X)/adjust;

end
```

Filtered Inversion QSM Algorithm

```
function [ X ] = WienerInverse( image,dx,dy,dz,orientation,S )
%Calculates the susceptibility in ppm from field shifts in muT.
%dx, dy, and dz are the resolution in x, y, and z in meters
%orientation is a string specifying the orientation of the object wrt the
%main field choices are 'axial' 'sagittal' or 'coronal'
%S is a positive number which controls the strength of the filtering effect, lower values of S
%indicate a stronger filter
dimension=size(image);
if size(dimension<4)
   dimension(4)=1;
end
H=salomirtf(dimension(1:3),dx,dy,dz,orientation);
SNR=ones(size(H))*abs(S);

H(abs(H)<=.0001)=.0001;

G= 1/H.*(abs(H).^2./(abs(H).^2+1/SNR));
adjust=sqrt( mean(mean(mean(abs(H.*G).^2))));
X=fftn(image);

for n=1:dimension(4)
X(:,:,:,n)=G.*X(:,:,:,n);
end
X=ifftn(X)/adjust;

end
```

Spatial Domain Regularization QSM Algorithm

```
%open corrected Bint nifti file
file=open_nifti;
%ensure even number of slices
dimension=size(file.img);

%check for odd dimensions;
%z direction
if mod(dimension(3),2)==1
   file.img=file.img(:,:,1:(dimension(3)-1));
   file.hdr.dime.dim(4)=file.hdr.dime.dim(4)-1;
end
%y direction
if mod(dimension(1),2)==1
   file.img=file.img(1:(dimension(1)-1),:,:);
   file.hdr.dime.dim(2)=file.hdr.dime.dim(2)-1;
end
%x direction
if mod(dimension(2),2)==1
   file.img=file.img(1:(dimension(2))-1,:,:);
   file.hdr.dime.dim(3)=file.hdr.dime.dim(3)-1;
end
dimension=size(file.img);%update dimension
%check for data sets with only one echo
if size(dimension)<4
   dimension=[dimension,1];
end

% % %open magnitude nifti file
file1=open_nifti;
file1.img=file1.img(:,:,:,1);
%ensure even number of slices
dimension=size(file1.img);

%check for odd dimensions;
%z direction
if mod(dimension(3),2)==1
   file1.img=file1.img(:,:,1:(dimension(3)-1));
   file1.hdr.dime.dim(4)=file1.hdr.dime.dim(4)-1;
end
%y direction
if mod(dimension(1),2)==1
   file1.img=file1.img(1:(dimension(1)-1),:,:);
   file1.hdr.dime.dim(2)=file1.hdr.dime.dim(2)-1;
end
%x direction
if mod(dimension(2),2)==1
   file1.img=file1.img(1:(dimension(2))-1,:,:);
   file1.hdr.dime.dim(3)=file1.hdr.dime.dim(3)-1;
end
dimension=size(file1.img);%update dimension
%check for data sets with only one echo
if size(dimension)<4
```

```
   dimension=[dimension,1];
end
% resolution in m
dy=file.hdr.dime.pixdim(2)/1000;
dx=file.hdr.dime.pixdim(3)/1000;
dz=file.hdr.dime.pixdim(4)/1000;

%% Set parameters for conjugate gradients regularization
x=zeros(dimension);%inital guess
M=ones(dimension);
M(file.img==0)=0;%mask for error term (positive mask ones inside the brain zeros outside the brain)
W0=1-M;%mask for regularization term (negative mask)
%W0=imdilate(logical(W0),strel('disk',8,8),'same');
M=1-W0;
%Create smoothness weighting based on SWI magnitude image
W=file1.img./mean(mean(mean(file1.img))).*(1-W0);%normalized magnitude image

W1x=convn(W,[1,-1],'valid');
W1y=convn(W,[1,-1]','valid');
z=ones(1,1,2);
z(:,:,2)=-1;
W1z=convn(W,z,'valid');
thresh=3*mean(mean(mean(abs(W1x))));
W1x(abs(W1x)<=thresh)=thresh;
W1y(abs(W1y)<=thresh)=thresh;
W1z(abs(W1z)<=thresh)=thresh;
W1x=(1/abs(W1x)).*(1-W0(:,1:end-1,:));
W1y=(1/abs(W1y)).*(1-W0(1:end-1,:,:));
W1z=(1/abs(W1z)).*(1-W0(:,:,1:end-1));

% W1x(isinf(W1x))=mean(mean(mean(W1x(~isinf(W1x)))));
% W1x(isnan(W1x))=0;
% W1x=W1x/mean(mean(mean(W1x)));
% W1y(isinf(W1y))=mean(mean(mean(W1y(~isinf(W1y)))));
% W1y(isnan(W1y))=0;
% W1y=W1y/mean(mean(mean(W1y)));
% W1z(isinf(W1z))=mean(mean(mean(W1z(~isinf(W1z)))));
% W1z(isnan(W1z))=0;

% W1z=W1z/mean(mean(mean(W1z)));
% gmask=ones(size(W1x));
% gmask(abs(W1x)<=.2)=0;
% W1x=imfilter(W1x,ones(5,5,5)/125).*gmask;
% gmask=ones(size(W1y));
% gmask(abs(W1y)<=.2)=0;
% W1y=imfilter(W1y,ones(5,5,5)/125).*gmask;
% gmask=ones(size(W1z));
% gmask(abs(W1z)<=.2)=0;
% W1z=imfilter(W1z,ones(5,5,5)/125).*gmask;

% mask=ones(size(W1x));
% mask(abs(W1x)>2*mean(mean(mean(abs(W1x)))))=0;
% W1x=mask;
% mask=ones(size(W1y));
% mask(abs(W1y)>2*mean(mean(mean(abs(W1y)))))=0;
```

```
% W1y=mask;
% mask=ones(size(W1z));
% mask(abs(W1z)>2*mean(mean(mean(abs(W1z)))))=0;
% W1z=mask;


n=250;%maximum iterations
a=15;%strength of regularization term
b=5;


H=salomirtf(dimension,dx,dy,dz,'coronal');
% t=.01;
% G=H;
% G(((abs(H)<=t)&(H<=0)))=-t;
% G(((abs(H)<=t)&(H>=0)))=t;
% adjust=sqrt( mean(mean(mean(abs(H./G).^2))));
% G=G*adjust;
[Xint]=LiuQSM(x,W,W0,W1x,W1y,W1z,H,file.img(:,:,:),a,b,n);
```

```
function [ x ] = LiuQSM( x,W,W0,W1x,W1y,W1z,H,dB,a,b,n )
%Function Description:
%This function uses conjugate gradients to find the solution to:
% minx ||W(Cx-d)||^2+a^2||W0x||^2+b^2||W1Gx||^2
%where Cx represents a 3D convolution in matrix vector form
%W, W0, W1 are diagonal matrices representing 3D image masks
%a controls the strength of the regularization term
%d is the observed solution to the convolution problem
%n is the maximum number of iterations
%% Intended Purpose
%although useable for any problem with the above form, this function was
%written expressly for the purpose of performing projection onto dipole
%filtering as a QSM preprocessing step to remove external field influences
%due to B0 or B1 inhomogeneity from unwrapped GRE phase images.
%The algorithm assumes C=C', as is the case for the unit dipole kernel!!

%% Function inputs

%Inputs W, W0, W1 are 3D masks of the brain. The mask can be based on the magnitude
%of the GRE image and used as a form of noise filtering, or it can be a
%straight mask of the brain so that only the residuals inside the brain are
%weighted. (Choose nonzero values inside the brain)

%Input H is a 3D matrix that describes the convolution kernel in the
%frequency domain

%d is a 3D matrix containing unwrapped GRE B0 maps

%a and b are a regularization parameter specifying the strength of the
%regularizing term

%n is the maximum number of iterations

%% Initialize vectors and parameters
i=0; %counts number of iterations
dimx=size(x);%find size of x
epsq=1E-10;%tolerance

%Compute residual (r=b-Ax) using FFTs
    %compute Gx'GxU
    GxGxU=convn(W1x.^2.*convn(x,[1,-1],'valid'),[-1,1],'full');
    %compute Gy'GyU
    GyGyU=convn(W1y.^2.*convn(x,[1,-1]','valid'),[-1,1]','full');
    %compute Gz'GzU
    z=ones(1,1,2);
    z(:,:,2)=-1;
    GzGzU=convn(W1z.^2.*convn(x,z,'valid'),-z,'full');
    gradpenalty=b^2*(GxGxU+GyGyU+GzGzU);

r=2*(ifftn(H.*fftn(W.^2.*dB))-ifftn(H.*fftn(W.^2.*ifftn(H.*fftn(x))))-a^2*W0.^2.*x-gradpenalty);
%initialize first and next search direction
d=r;
dnew=sum(sum(sum(r.^2)));%r'*r;
d0=dnew;
```

```
%DIAGNOSTICS
progress=zeros(dimx(1),dimx(2),n);
cost=zeros(3,n);
%iterate
while i<n && dnew>epsq*d0
   %calculate q=Ad using FFTs
      %compute Gx'GxU
      GxGxd=convn(W1x.^2.*convn(d,[1,-1],'valid'),[-1,1],'full');
      %compute Gy'GyU
      GyGyd=convn(W1y.^2.*convn(d,[1,-1]','valid'),[-1,1]','full');
      %compute Gz'GzU
      z=ones(1,1,2);
      z(:,:,2)=-1;
      GzGzd=convn(W1z.^2.*convn(d,z,'valid'),-z,'full');
      gradpenalty=b^2*(GxGxd+GyGyd+GzGzd);
   q=2*(ifftn(H.*fftn(W.^2.*ifftn(H.*fftn(d))))+a^2*W0.^2.*d+gradpenalty);

   %%Calculate how far to make next guess
   alpha=dnew/sum(sum(sum(double(d).*double(q))));%calculate how far to make next guess

   x=x+alpha*d;

   if ceil(i/50)==i/50 && i~=0 %if divisible by 50 reinitialize residual vector
      %Compute residual (r=b-Ax) using FFTs
      %compute Gx'GxU
      GxGxU=convn(W1x.^2.*convn(x,[1,-1],'valid'),[-1,1],'full');
      %compute Gy'GyU
      GyGyU=convn(W1y.^2.*convn(x,[1,-1]','valid'),[-1,1]','full');
      %compute Gz'GzU
      z=ones(1,1,2);
      z(:,:,2)=-1;
      GzGzU=convn(W1z.^2.*convn(x,z,'valid'),-z,'full');
      gradpenalty=b^2*(GxGxU+GyGyU+GzGzU);
      r=2*(ifftn(H.*fftn(W.^2.*dB))-ifftn(H.*fftn(W.^2.*ifftn(H.*fftn(x))))-a^2*W0.^2.*x-gradpenalty);
   else
      r=r-alpha*q;
   end
      dold=dnew;
      dnew=sum(sum(sum(r.^2)));
      beta=dnew/dold;
      d=r+beta*d;
      i=i+1
end
end
```

APPENDIX B: EXAM CARDS

Multiple Sclerosis Images

Hospital (1) | MS_Protocol (1) | H23_MS034 (14) 47:36.3 | 3D_FFE0.6isoallHead SENSE 08:48.0

INFO PAGE	
Total scan duration	08:48.0
Rel. signal level (%)	100
Act. TR/TE1/delta TE (ms)	30 / 3.1 / 4.3
ACQ matrix M x P	332 x 293
ACQ voxel MPS (mm)	0.60 / 0.60 / 1.20
REC voxel MPS (mm)	0.60 / 0.59 / 0.60
Scan percentage (%)	100.6711
Act. WFS (pix) / BW (Hz)	4.018 / 252.2
Min. WFS (pix) / Max. BW (Hz)	1.000 / 1013.1
Min. TR/TE1/delta TE (ms)	24 / 3.1 / 4.3
RF avg power computed (W)	0.1616655
SAR / head	< 2 % / 0.1 W/kg
Head / level	< 0.1 W/kg / normal
B1 rms [uT]	0.1966218
PNS / level	64 % / normal

MOTION	
Cardiac synchronization	no
Respiratory compensation	no
Navigator respiratory comp	no
Flow compensation	no
fMRI echo stabilisation	no
NSA	1

DYN/ANG	
Angio	no
Quantitative flow	no
Manual start	no
Dynamic study	no
Flow labeling	none

POST/PROC	
Preparation phases	full
Manual Offset Freq.	no
SENSE ref. scan	no
SmartPlan scout	no
B0 field map/Dixon	no
B1 field map	no
MIP/MPR	no
Images	M, R, I, no
Autoview image	M
Calculated images	no, no, no, no
Reference tissue	Grey matter
Preset window contrast	soft
Reconstruction mode	immediate
Save raw data	yes
Hardcopy protocol	no
Ringing filtering	yes
Geometry correction	default
Elliptical k-space shutter	default

GEOMETRY	
Nucleus	H1
Coil selection	SENSE-Head-7T
Xmit Coil selection	Volume-T/R
element selection	All
connection	d
Dual coil	no
CLEAR	yes
body tuned	no
SENSE	yes
P reduction (RL)	2
P os factor	1
S reduction (FH)	1
k-t BLAST	no
FOV AP (mm)	200
RL (mm)	176.1905
FH (mm)	142.2
Voxel size AP (mm)	0.6
RL (mm)	0.6
FH (mm)	0.6
Recon voxel size (mm)	0.6
Reconstruction matrix	336
Overcontiguous slices	yes
Stacks	1
slices	237
slice orientation	transverse
fold-over direction	RL
fat shift direction	P
Fold-over suppression	no
Slice oversampling	default
Chunks	1
PlanAlign	no
REST slabs	0
Catheter tracking	no
Interactive positioning	no
Allow table movement	no

OFFC/ANG	
Stacks	1
Stack Offc. AP (P=+mm)	-2.320078
RL (L=+mm)	-6.504592
FH (H=+mm)	-1.489353
Ang. AP (deg)	-1.840552
RL (deg)	17.44282
FH (deg)	-1.378752

CONTRAST	
Scan type	Imaging
Scan mode	3D
technique	FFE
Contrast enhancement	T1
Acquisition mode	cartesian
Fast Imaging mode	none
Echoes	5
partial echo	no
shifted echo	no
TE first	shortest
echospacing	shortest
flyback	no
Flip angle (deg)	5
TR	user defined
(ms)	29.5
Halfscan	no
Water-fat shift	user defined
(pixels)	4
Shim	default
Fat suppression	no
Water suppression	no
MTC	no
Research prepulse	no
Diffusion mode	no
SAR mode	high
B1 mode	default
PNS mode	high
Gradient mode	maximum
SofTone mode	no

Short TE Scaling Example

Hospital (2) | Sharon (1) | phase_111 (13) 46:30.6 | SWI_s2_0.5x0.5x0.5_SNR 11:40.0

INFO PAGE	
Total scan duration	11:40.0
Rel. signal level (%)	100
Act. TR/TE1/delta TE (ms)	34 / 5.0 / 5.0
ACQ matrix M x P	440 x 401
ACQ voxel MPS (mm)	0.50 / 0.50 / 0.50
REC voxel MPS (mm)	0.49 / 0.49 / 0.50
Scan percentage (%)	100.4926
Act. WFS (pix) / BW (Hz)	4.510 / 224.7
Min. WFS (pix) / Max. BW (Hz)	1.190 / 851.5
Min. TR/TE1/delta TE (ms)	34 / 3.4 / 4.8
RF avg power computed (W)	0.1681224
SAR / head	< 2 %
Head / level	< 0.1 W/kg / normal
B1 rms	0.18 uT
PNS / level	34 % / normal
Sound Pressure Level (dB)	27.6209

MOTION	
Cardiac synchronization	no
Heart rate > 250 bpm	no
Respiratory compensation	no
Navigator respiratory comp	no
Flow compensation	no
fMRI echo stabilisation	no
NSA	1

DYN/ANG	
Angio / Contrast enh.	no
Quantitative flow	no
Manual start	no
Dynamic study	no
Arterial Spin labeling	no

POST/PROC	
Preparation phases	full
Interactive F0	no
SENSE ref. scan	no
SmartPlan survey	no
B0 field map	no
B1 field map	no
MIP/MPR	no
Images	M, R, I, no
Autoview image	M
Calculated images	no, no, no, no
Reference tissue	Grey matter
Preset window contrast	soft
Reconstruction mode	immediate
Save raw data	no
Hardcopy protocol	no
Ringing filtering	rectangular
Geometry correction	default
Elliptical k-space shutter	default

GEOMETRY	
Nucleus	H1
Coil selection	SENSE-Head-7T
Xmit Coil selection	Volume-T/R
element selection	All
connection	d
Dual coil	no
CLEAR	yes
body tuned	no
FOV FH (mm)	220
AP (mm)	200.3571
RL (mm)	50
Voxel size FH (mm)	0.5
AP (mm)	0.5
RL (mm)	0.5
Recon voxel size (mm)	0.5
Fold-over suppression	no
Slice oversampling	default
RF select. FOS	no
Reconstruction matrix	448
SENSE	yes
P reduction (AP)	2
P os factor	1
S reduction (RL)	1
k-t BLAST	no
Overcontiguous slices	no
Stacks	1
slices	100
slice orientation	sagittal
fold-over direction	AP
fat shift direction	F
Chunks	1
PlanAlign	no
REST slabs	0
Catheter tracking	no
Interactive positioning	no
Allow table movement	no

OFFC/ANG	
Stacks	1
Stack Offc. AP (P=+mm)	-6.823566
RL (L=+mm)	1.291543
FH (H=+mm)	-15.38839
Ang. AP (deg)	1.368177
RL (deg)	1.242744E-17
FH (deg)	5.838265

CONTRAST	
Scan type	Imaging
Scan mode	3D
technique	FFE
loop order	zy_order
Contrast enhancement	no
Acquisition mode	cartesian
Fast Imaging mode	none
3D non-selective	no
Echoes	6
partial echo	no
shifted echo	no
TE first	user defined
(ms)	5
echospacing	user defined
(ms)	5
flyback	no
Flip angle (deg)	5
TR	shortest
Halfscan	no
Water-fat shift	user defined
(pixels)	4.5
Shim	default
mDIXON	no
Fat suppression	no
Water suppression	no
MTC	no
Research prepulse	no
Diffusion mode	no
SAR mode	high
B1 mode	default
SAR Patient data	auto
PNS mode	high
Gradient mode	maximum
SofTone mode	no

Hospital (2) | Sharon (1) | phase_111 (13) 46:30.6 | 3dffe_bo_1x1x1_TE1.34 00:51.2

INFO PAGE	
Total scan duration	00:51.2
Rel. signal level (%)	100
Act. TR/TE1/delta TE (ms)	10 / 1.36 / 1.1
ACQ matrix M x P	220 x 200
ACQ voxel MPS (mm)	1.00 / 1.00 / 1.00
REC voxel MPS (mm)	0.49 / 0.49 / 1.00
Scan percentage (%)	100
Act. WFS (pix) / BW (Hz)	0.612 / 1657.0
Min. WFS (pix) / Max. BW (Hz)	0.595 / 1703.1
Min. TR/TE1/delta TE (ms)	6.1 / 1.36 / 1.06
RF avg power computed (W)	0.5742979
SAR / head	< 7 %
Head / level	< 0.2 W/kg / normal
B1 rms	0.34 uT
PNS / level	65 % / normal
Sound Pressure Level (dB)	40.58863

MOTION	
Cardiac synchronization	no
Heart rate > 250 bpm	no
Respiratory compensation	no
Navigator respiratory comp	no
Flow compensation	no
fMRI echo stabilisation	no
NSA	1

DYN/ANG	
Angio / Contrast enh.	no
Quantitative flow	no
Manual start	no
Dynamic study	no
Arterial Spin labeling	no

POST/PROC	
Preparation phases	full
Interactive F0	no
SENSE ref. scan	no
SmartPlan survey	no
B0 field map	no
B1 field map	no
MIP/MPR	no
Images	M, R, I, P
Autoview image	M
Calculated images	no, no, no, no
Reference tissue	Grey matter
Preset window contrast	soft
Reconstruction mode	immediate
Save raw data	no
Hardcopy protocol	no
Ringing filtering	rectangular
Geometry correction	default
Elliptical k-space shutter	default

GEOMETRY	
Nucleus	H1
Coil selection	SENSE-Head-7T
Xmit Coil selection	Volume-T/R
element selection	All
connection	d
Dual coil	no
CLEAR	yes
body tuned	no
FOV FH (mm)	220
AP (mm)	200.3571
RL (mm)	50
Voxel size FH (mm)	1
AP (mm)	1.003968
RL (mm)	1
Recon voxel size (mm)	0.5
Fold-over suppression	no
Slice oversampling	default
RF select. FOS	no
Reconstruction matrix	448
SENSE	yes
P reduction (AP)	2
P os factor	1
S reduction (RL)	1
k-t BLAST	no
Overcontiguous slices	no
Stacks	1
slices	50
slice orientation	sagittal
fold-over direction	AP
fat shift direction	F
Chunks	1
PlanAlign	no
REST slabs	0
Catheter tracking	no
Interactive positioning	no
Allow table movement	no

OFFC/ANG	
Stacks	1
Stack Offc. AP (P=+mm)	-6.823566
RL (L=+mm)	1.291543
FH (H=+mm)	-15.38839
Ang. AP (deg)	1.368177
RL (deg)	1.242744E-17
FH (deg)	5.838265

CONTRAST	
Scan type	Imaging
Scan mode	3D
technique	FFE
loop order	zy_order
Contrast enhancement	no
Acquisition mode	cartesian
Fast Imaging mode	none
3D non-selective	no
Echoes	4
partial echo	no
shifted echo	no
TE first	shortest
echospacing	shortest
flyback	no
Flip angle (deg)	5
TR	user defined
(ms)	10
Halfscan	no
Water-fat shift	minimum
Shim	default
mDIXON	no
Fat suppression	no
Water suppression	no
MTC	no
Research prepulse	no
Diffusion mode	no
SAR mode	high
B1 mode	default
SAR Patient data	auto
PNS mode	high
Gradient mode	maximum
SofTone mode	no

Hospital (2) | Sharon (1) | phase_111 (13) 46:30.6 | 3dffe_bo_1x1x1_TE1.55 00:51.2

INFO PAGE	
Total scan duration	00:51.2
Rel. signal level (%)	100
Act. TR/TE1/delta TE (ms)	10 / 1.55 / 1.1
ACQ matrix M x P	220 x 200
ACQ voxel MPS (mm)	1.00 / 1.00 / 1.00
REC voxel MPS (mm)	0.49 / 0.49 / 1.00
Scan percentage (%)	100
Act. WFS (pix) / BW (Hz)	0.612 / 1657.0
Min. WFS (pix) / Max. BW (Hz)	0.595 / 1703.1
Min. TR/TE1/delta TE (ms)	6.3 / 1.36 / 1.06
RF avg power computed (W)	0.5742979
SAR / head	< 7 %
Head / level	< 0.2 W/kg / normal
B1 rms	0.34 uT
PNS / level	65 % / normal
Sound Pressure Level (dB)	39.9283

MOTION	
Cardiac synchronization	no
Heart rate > 250 bpm	no
Respiratory compensation	no
Navigator respiratory comp	no
Flow compensation	no
fMRI echo stabilisation	no
NSA	1

DYN/ANG	
Angio / Contrast enh.	no
Quantitative flow	no
Manual start	no
Dynamic study	no
Arterial Spin labeling	no

POST/PROC	
Preparation phases	full
Interactive F0	no
SENSE ref. scan	no
SmartPlan survey	no
B0 field map	no
B1 field map	no
MIP/MPR	no
Images	M, R, I, P
Autoview image	M
Calculated images	no, no, no, no
Reference tissue	Grey matter
Preset window contrast	soft
Reconstruction mode	immediate
Save raw data	no
Hardcopy protocol	no
Ringing filtering	rectangular
Geometry correction	default
Elliptical k-space shutter	default

GEOMETRY	
Nucleus	H1
Coil selection	SENSE-Head-7T
Xmit Coil selection	Volume-T/R
element selection	All
connection	d
Dual coil	no
CLEAR	yes
body tuned	no
FOV FH (mm)	220
AP (mm)	200.3571
RL (mm)	50
Voxel size FH (mm)	1
AP (mm)	1.003968
RL (mm)	1
Recon voxel size (mm)	0.5
Fold-over suppression	no
Slice oversampling	default
RF select. FOS	no
Reconstruction matrix	448
SENSE	yes
P reduction (AP)	2
P os factor	1
S reduction (RL)	1
k-t BLAST	no
Overcontiguous slices	no
Stacks	1
slices	50
slice orientation	sagittal
fold-over direction	AP
fat shift direction	F
Chunks	1
PlanAlign	no
REST slabs	0
Catheter tracking	no
Interactive positioning	no
Allow table movement	no

OFFC/ANG	
Stacks	1
Stack Offc. AP (P=+mm)	-6.823566
RL (L=+mm)	1.291543
FH (H=+mm)	-15.38839
Ang. AP (deg)	1.368177
RL (deg)	1.242744E-17
FH (deg)	5.838265

CONTRAST	
Scan type	Imaging
Scan mode	3D
technique	FFE
loop order	zy_order
Contrast enhancement	no
Acquisition mode	cartesian
Fast Imaging mode	none
3D non-selective	no
Echoes	4
partial echo	no
shifted echo	no
TE first	user defined
(ms)	1.55
echospacing	shortest
flyback	no
Flip angle (deg)	5
TR	user defined
(ms)	10
Halfscan	no
Water-fat shift	minimum
Shim	default
mDIXON	no
Fat suppression	no
Water suppression	no
MTC	no
Research prepulse	no
Diffusion mode	no
SAR mode	high
B1 mode	default
SAR Patient data	auto
PNS mode	high
Gradient mode	maximum
SofTone mode	no

MR Phantoms

Hospital (2) | Sharon (1) | pink_ballon (8) 40:12.9 | 3dffe_mTEmindTEmin 04:54.7

INFO PAGE	
Total scan duration	04:54.7
Rel. signal level (%)	100
Act. TR/TE1/TE2 (ms)	12 / 1.54 / 2.8
ACQ matrix M x P	240 x 160
ACQ voxel MPS (mm)	0.75 / 0.75 / 0.75
REC voxel MPS (mm)	0.75 / 0.75 / 0.75
Scan percentage (%)	100
Act. WFS (pix) / BW (Hz)	0.806 / 1257.1
Min. WFS (pix) / Max. BW (Hz)	0.793 / 1277.3
Min. TR/TE1/TE2 (ms)	4.6 / 1.54 / 2.8
RF avg power computed (W)	0.1422621
SAR / local torso	< 6 %
Whole body / level	0.0 W/kg / normal
B1 rms	0.31 uT
PNS / level	70 % / normal
Sound Pressure Level (dB)	35.20409
MOTION	
Cardiac synchronization	no
Heart rate > 250 bpm	no
Respiratory compensation	no
Navigator respiratory comp	no
Flow compensation	no
fMRI echo stabilisation	no
NSA	1
DYN/ANG	
Angio / Contrast enh.	no
Quantitative flow	no
Manual start	no
Dynamic study	no
Arterial Spin labeling	no
POST/PROC	
Preparation phases	sameprep
Interactive F0	no
SENSE ref. scan	no
SmartPlan survey	no
B0 field map	no
B1 field map	no
MIP/MPR	no
Images	M, R, I, P
Autoview image	M
Calculated images	no, no, no, no
Reference tissue	Grey matter
Preset window contrast	soft
Reconstruction mode	immediate
Save raw data	no
Hardcopy protocol	no
Ringing filtering	rectangular
Geometry correction	default
Elliptical k-space shutter	default

GEOMETRY	
Multi-transmit	no
Nucleus	H1
Coil selection	RX-Intf-1
Xmit Coil selection	MTX-Volume-T/R
User def elem sel	no
element selection	All
connection	d
Dual coil	no
CLEAR	yes
body tuned	no
FOV FH (mm)	180
RL (mm)	120
AP (mm)	120
Voxel size FH (mm)	0.75
RL (mm)	0.75
AP (mm)	0.75
Recon voxel size (mm)	0.75
Fold-over suppression	no
Slice oversampling	default
RF select. FOS	no
Reconstruction matrix	240
SENSE	no
k-t BLAST	no
Overcontiguous slices	no
Stacks	1
slices	160
slice orientation	coronal
fold-over direction	RL
fat shift direction	F
Chunks	1
PlanAlign	no
REST slabs	0
Catheter tracking	no
Interactive positioning	no
Allow table movement	no
OFFC/ANG	
Stacks	1
Stack Offc. AP (P=+mm)	5.104091
RL (L=+mm)	4.962117
FH (H=+mm)	-25.33069
Ang. AP (deg)	0
RL (deg)	0
FH (deg)	0
Shim Size AP (mm)	61.74033
RL (mm)	67.65575
FH (mm)	145.2048
Offc. AP (P=+mm)	3.289207
RL (L=+mm)	5.277123
FH (H=+mm)	-23.04358
Ang. AP (deg)	0
RL (deg)	0
FH (deg)	-0.1072408

CONTRAST	
Scan type	Imaging
Scan mode	3D
technique	FFE
loop order	zy_order
Contrast enhancement	no
Acquisition mode	cartesian
Fast Imaging mode	none
3D non-selective	no
Echoes	2
partial echo	no
shifted echo	no
TE first	shortest
second	shortest
flyback	no
Flip angle (deg)	5
TR	user defined
(ms)	11.5
Halfscan	no
Water-fat shift	minimum
Shim	PB-volume
ShimAlign	no
mDIXON	no
Fat suppression	no
Water suppression	no
MTC	no
Research prepulse	no
Diffusion mode	no
SAR mode	high
B1 mode	default
SAR Patient data	auto
PNS mode	high
Gradient mode	maximum
SofTone mode	no